Generalized finite element method enrichment functions for curved singularities in 3D fracture mechanics problems

J.P. Pereira[†], C.A. Duarte[†],[*], X. Jiao[††] and D. Guoy[‡]

November 28, 2008

[†]*Department of Civil & Environmental Engineering,*

University of Illinois at Urbana-Champaign, 205 North Mathews Ave., Urbana, IL 61801, U.S.A..

[††]*Department of Applied Mathematics and Statistics, Stony Brook University, Stony Brook, NY 11794-3600.*

[‡]*Center for Simulation of Advanced Rockets,*

University of Illinois at Urbana-Champaign, 1304 West Springfield Avenue, Urbana, IL 61801, U.S.A..

Abstract

This paper presents a study of generalized enrichment functions for three-dimensional curved crack fronts. Two coordinate systems used in the definition of singular curved crack front enrichment functions are analyzed. In the first one, a set of Cartesian coordinate systems defined along the crack front is used. In the second case, the geometry of the crack front is approximated by a set of curvilinear coordinate systems. A description of the computation of derivatives of enrichment functions and curvilinear base vectors is presented. The coordinate systems are automatically defined using geometrical information provided by an explicit representation of the crack surface. A detailed procedure to accurately evaluate the surface normal, conormal and tangent vectors along curvilinear crack fronts in explicit crack surface representations is also presented. An accurate and robust definition of orthonormal vectors along crack fronts is crucial for the proper definition of enrichment functions. Numerical experiments illustrate the accuracy and robustness of the proposed approaches.

Keywords: Partition of unity methods; Generalized/Extended finite element method; Three-dimensional fracture mechanics; Crack front enrichments.

1 Introduction

Three-dimensional computational fracture mechanics simulations are of great importance in industry. Life prediction of engine components, structural members of aircraft fuselage, and pipeline joints are examples of industrial problems in which 3D computational fracture mechanics analysis is broadly applied. The standard finite element method (FEM) has been used for several decades in the assessment of such industrial problems. The application of the FEM to this class of problems faces several issues regarding changes in mesh topology and excessive computational cost. These difficulties are usually due to remeshing and the need for highly refined meshes in the crack surface region. Such modifications in the mesh are often required because of crack surface fitting and accuracy of the solution. Partition of unity methods, such as the generalized finite element method (GFEM) [1, 4, 16, 23, 33], are promising candidates to overcome

---

[*]Corresponding author: caduarte@illinois.edu

these difficulties. However, in three-dimensional fracture analysis with partition of unity-based methods, the accurate representation of curvilinear crack fronts is still a challenging task.

Partition of unity methods have been successfully applied to fracture mechanics problems. The main idea of modeling fracture mechanics problems with these methods is to represent discontinuities and singularities of the solution through custom-built shape functions. The discontinuity far from crack tip/front can be easily represented by step functions [19, 20, 35] or high-order step functions [6, 28], depending on the polynomial order used in the approximation of the continuous part of the solution. In order to represent the singularity of the solution in linear elastic fracture mechanics problems, enrichment functions based on the analytical solution of the elasticity around the crack front are usually applied [2, 4, 5, 20, 22, 24, 28, 35]. The application of partition of unity methods to cohesive fracture models and corresponding enrichments can be found in, for example, [17, 18, 31, 32, 40, 41, 42].

In the mid 1990's, many researchers applied the partition of unity concept and the asymptotic expansion near the crack tip to represent discontinuities and singularities in two-dimensional crack problems. The idea of including the near crack tip asymptotic expansion in partition of unity approximation was firstly introduced by Duarte and Oden in [7, 22, 24]. They used the partition of unity concept in the *hp*-cloud method to represent the singularity and discontinuity of the solution in the approximation. Asymptotic expansions were introduced in the element-free Galerkin method by Fleming et al. [9]. Two approaches were utilized to enrich the element-free Galerkin approximation with the first terms of the near tip expansion. The first approach adds the first terms of the near-tip asymptotic expansion of the displacement field to the trial functions. The second approach expands the linear basis used in the moving least squares method [13, 14] by including the term $\sqrt{r}$ multiplied by trigonometric functions. By using the partition of unity concept, Belytschko and Black [2] applied the second enrichment approach introduced in [9] in a finite element framework. The approach introduced by Belytschko and Black [2] was improved by Moës et al. [19]. They applied Heaviside functions to those nodes with support intersecting the crack surface but not the crack tip, and the asymptotic expansion for those nodes with support intersecting the crack tip.

Duarte et al. [4] extended the enrichment approach used in [7, 22, 24] for a three-dimensional finite element framework. The asymptotic expansion was utilized to model straight reentrant corners using the partition of unity concept. In [5], Duarte et al. applied the same enrichment approach to arbitrary crack fronts in three-dimensional dynamic crack propagation. Sukumar et al. [35] and Moës et al. [20] extended the approach presented in [19] for three-dimensional crack modeling of planar and non-planar crack surfaces with curved crack fronts, respectively.

To our best knowledge, the references available in the literature regarding three-dimensional analysis of crack problems using partition of unity-based methods, give very little attention to the description and construction of enrichment functions for curved fronts. Moreover, in all existing approaches, the effects of crack front curvatures in the asymptotic expansion are not considered in the enrichment functions.

The aim of this paper is to analyze two approaches for describing and enriching three-dimensional curved crack fronts. The first approach is based on a piecewise linear description of the crack front. The second one uses a piecewise quadratic description while taking into consideration the derivatives of the base vectors in the computation of the gradient of the asymptotic expansion. Another contribution of this paper is a detailed procedure to evaluate surface normal, conormal and tangent vectors along a curved crack front. These vectors are utilized in the definition of base vectors which, in turn, define the crack front enrichment functions. An accurate and robust definition of these crack front vectors is crucial for the proper definition of crack front enrichment functions.

The outline of this paper is as follows. In the following Section we briefly review the construction of GFEM shape functions and present the enrichment functions used with the proposed piecewise linear and quadratic crack front geometrical approximations. Section 3 presents a procedure to accurately evaluate

the normal, conormal and tangent vectors along the crack front in an explicit crack surface representation. The crack front description using linear and quadratic approximations and the transformation maps for their respective enrichment functions are discussed in Section 4. The numerical experiments presented in Section 5 illustrate the robustness and accuracy of the proposed three-dimensional enrichment techniques. Finally, Section 6 outlines the conclusions and highlights the main contributions of the present study.

2 Generalized FE shape functions

The generalized FEM [1, 4, 16, 23, 33] can be regarded as a FEM with shape functions built using the concept of a partition of unity. In this section, we focus on the construction of GFEM shape functions used in the neighborhood of a three-dimensional crack front. Details on the GFEM can be found in many papers available in the literature. Here, we follow the formulation and notation introduced in [28].

In the GFEM, a shape function $\phi_{\alpha i}$ is built from the product of a linear finite element shape function, φ_α, and an enrichment function, $L_{\alpha i}$,

$$\phi_{\alpha i}(\boldsymbol{x}) = \varphi_\alpha(\boldsymbol{x}) L_{\alpha i}(\boldsymbol{x}) \qquad \text{(no summation on } \alpha\text{)} \tag{1}$$

where α is the index of a node $\boldsymbol{x}_\alpha$ in the finite element mesh. The GFEM shape function $\phi_{\alpha i}$ is defined on $\omega_\alpha = \{\boldsymbol{x} \in \Omega : \varphi_\alpha(\boldsymbol{x}) \neq 0\}$, the support of the partition of unity function φ_α. In the case of a finite element partition of unity, the support ω_α (often called cloud) is given by the union of the finite elements sharing a vertex node $\boldsymbol{x}_\alpha$ [4]. The selection of enrichment functions depends on the local behavior of the solution $\boldsymbol{u}$ of the problem of interest over the cloud ω_α. In the case of linear elastic fracture mechanics problems, the enrichment functions used at clouds ω_α that intersect the crack front are taken from the asymptotic expansion of the elasticity solution near a crack front [4, 5, 22, 24, 28].

Let ξ_1, ξ_2 and ξ_3 denote directions in a curvilinear coordinate system defined along the crack front as illustrated in Figure 1. Directions ξ_1, ξ_2 and ξ_3 are in the forward direction of the crack front, perpendicular to the crack surface and tangent to the crack front, respectively. A curvilinear cylindrical coordinate system with coordinates r, θ and ξ_3 is also illustrated in Figure 1.
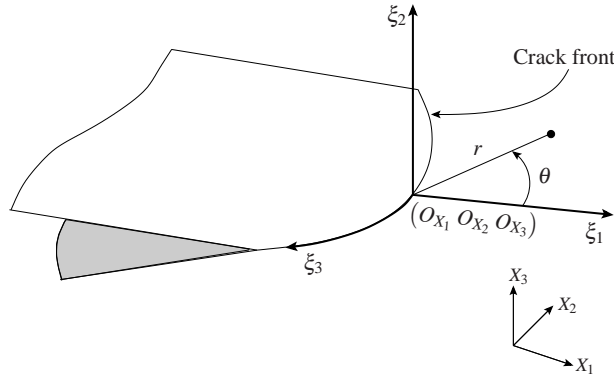

Figure 1: Curvilinear orthogonal coordinate system defined along a curved crack front. This coordinate system is used in the computation of enrichment functions defined in (2).

The enrichment functions used to approximate displacement fields in the ξ_1, ξ_2 and ξ_3 directions are

3

given by [4, 5, 22, 24, 28]

$$\begin{aligned}
\bar{L}^{\xi_1}_{\alpha 1}(r,\theta) &= \sqrt{r}\left[\left(\kappa-\frac{1}{2}\right)\cos\frac{\theta}{2}-\frac{1}{2}\cos\frac{3\theta}{2}\right]\\
\bar{L}^{\xi_2}_{\alpha 1}(r,\theta) &= \sqrt{r}\left[\left(\kappa+\frac{1}{2}\right)\sin\frac{\theta}{2}-\frac{1}{2}\sin\frac{3\theta}{2}\right]\\
\bar{L}^{\xi_3}_{\alpha 1}(r,\theta) &= \sqrt{r}\sin\frac{\theta}{2}\\
\bar{L}^{\xi_1}_{\alpha 2}(r,\theta) &= \sqrt{r}\left[\left(\kappa+\frac{3}{2}\right)\sin\frac{\theta}{2}+\frac{1}{2}\sin\frac{3\theta}{2}\right]\\
\bar{L}^{\xi_2}_{\alpha 2}(r,\theta) &= \sqrt{r}\left[\left(\kappa-\frac{3}{2}\right)\cos\frac{\theta}{2}+\frac{1}{2}\cos\frac{3\theta}{2}\right]\\
\bar{L}^{\xi_3}_{\alpha 2}(r,\theta) &= \sqrt{r}\sin\frac{3\theta}{2}
\end{aligned} \tag{2}$$

where the material constant $\kappa = 3 - 4\nu$ and ν is Poisson's ratio. This assumes plane strain conditions, which is in general a good approximation far from crack front ends. The above enrichment functions correspond to the first term of the modes *I* and *II*, and to the first and second terms of the mode *III* components of the asymptotic expansion of elasticity solution around a straight crack front, far from the vertices and for a traction-free flat crack surface [36]. It should be noted, as indicated by the superscripts, that different enrichment functions are used in (2) for each component of the displacement vector. This leads to a total of six additional degrees of freedom at a node α enriched with these functions. In contrast, the enrichment functions used in, e.g., [3, 20, 34, 35], lead, in 3D, to twelve degrees of freedom per node since four enrichment functions are used for each component of the displacement vector. In the approach proposed in (2), only two enrichments are used to enrich each component of the displacement vector. The performance of these two choices of enrichment functions is analyzed in [25].

The enrichment functions (2) are defined in a coordinate system located along the crack front as illustrated in Figure 1. Thus, they must be transformed to the global Cartesian coordinate system (X_1, X_2, X_3) prior to their use in the definition of GFEM shape functions in (1). Details are presented in Sections 4.1.1 and 4.2.2.

In our computations, the crack surface is represented by flat triangles with straight edges [28] as illustrated in Figures 5 and 6. Thus, curved crack fronts are approximated by straight line segments. The fidelity of this approximation can be controlled by simply using a finer triangulation of the crack surface. This process is *independent* of the GFEM mesh and does not change the problem size [28]. This paper focus on the construction of crack front coordinate systems and corresponding enrichment functions using geometrical information provided by this crack surface representation. It should be noted that the coordinate systems proposed here can be used to define enrichment functions for several classes of problems. In particular, it can be applied to the case of cohesive cracks, and other non-linear fracture mechanics problems. The only modification required is to replace (2) by appropriate enrichment functions.

3 Crack front base vectors

This section presents computational procedures to determine orthonormal base vectors at vertices along a crack front. These crack front vectors are the surface normal vector, curve tangent vector and conormal vector computed at each vertex of the front using the geometrical description of the crack surface. These vectors define a local Cartesian coordinate system at each crack front vertex. Moreover, they are utilized

in the construction of curved hexahedra along the crack front. These elements, in turn, define curvilinear coordinate systems, as described in Section 4.2.1.

3.1 Evaluation of the crack front normals, tangent and conormal vectors

The crack front normal, tangent and conormal vectors are used in the definition of the branch function enrichments (2) as well as in the extraction of stress intensity factors (SIFs). A good estimation of these crack front vectors is worthwhile to obtain an accurate approximation of the solution around the crack front and, consequently, an accurate SIF extraction.

In the level sets method applied to partition of unit-based methods for crack problems [20, 34, 35], the crack front vectors of the implicit representation of the crack surface are computed based on the gradients of the front and surface level sets. However, according to Duflot [8], this approach may lead to an inaccurate representation of the crack front because the orthogonality of the surface and front level set gradients does not always hold.

In this paper, the crack surface is represented by an explicit three-dimensional triangulation. Figure 2 illustrates an arbitrary crack surface and the normal, tangent and conormal vectors along the crack front. More details about this crack surface representation can be found in [28]. The evaluation of the crack front vectors for this explicit representation of the crack surface, by design, guarantees the accuracy and orthogonality of the crack front vectors. The following sequence of procedures describes how to evaluate the crack front normals for an explicit crack surface representation.
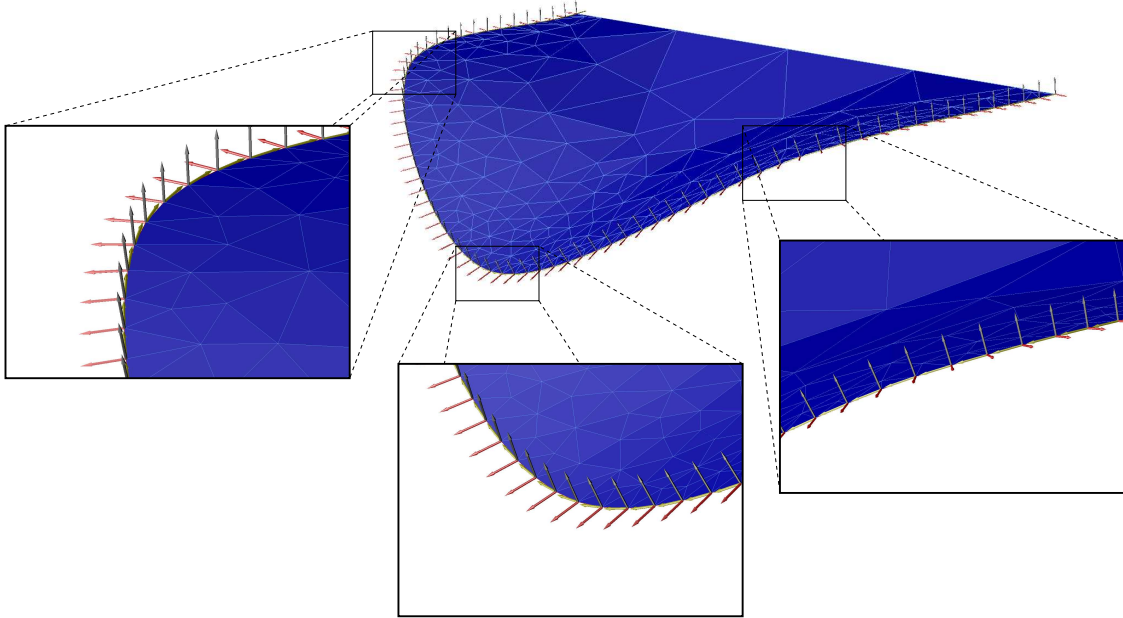

Figure 2: Non-planar crack surface and normals, tangents and conormals along the crack front represented by black, yellow and red arrows, respectively..

Evaluation of the normal vectors using medial quadric   The computation of normal vectors at vertices of facets representing a C^0 surface is not a trivial task. The vertex normals along the crack front are ill-defined and an algorithm based on a naive approach, e.g. the average of normals of the facets sharing a vertex, may lead to inaccurate estimates of normals for coarse meshes or near geometric singularities. Figure

3 illustrates a comparison among vertex normals computed with weighted-averaging, first eigenvector of covariance matrix and the approach used in this paper.

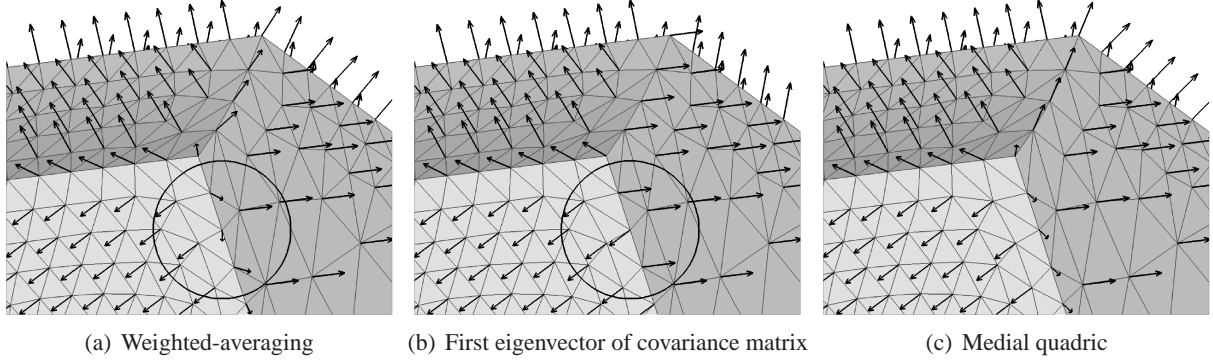(a) Weighted-averaging   (b) First eigenvector of covariance matrix   (c) Medial quadric

Figure 3: Comparison of estimated normals along ridges using different techniques, all weighted by area.

The computation of the normal vectors adopted here is based on the eigenvalue analysis of the *offset quadric* [10]. This procedure is used in the Face Offsetting Method (FOM) [10] to reconstruct the vertices of an evolving surface as well as for normal computation in [11]. In this paper, we adapt the method to the case of normal evaluation along the boundary of a surface, the crack front in this case.

In order to find an estimate of the normal vector at a given vertex v_j along the crack front, a unity movement $\boldsymbol{\delta}_i$ is applied to the facets connected to that vertex in the direction of their normals. Next, the intersection of the planes represented by the facets at their new positions is computed in a least-square sense. The intersection is the point that minimizes the sum of the squared distances to the planes. The *offset quadric* is then formulated as follows.

Given a plane γ_i with unit normal $\bar{\boldsymbol{n}}_i$ and an arbitrary point $\boldsymbol{y} \in \gamma_i$, the signed distance of the plane to the origin is given by $\delta_i = -\boldsymbol{y} \cdot \bar{\boldsymbol{n}}_i$ which can be regarded as the movement of the plane with respect to its initial position towards its normal direction. The orientation of the plane γ_i is defined by the cyclic order of the facet connectivities. This information is provided by the triangulation that describes the crack surface. The distance of an arbitrary point $\boldsymbol{x} \in \Re^3$ to the plane γ_i can be written as (cf. Figure 4(a))

$$h(\boldsymbol{x}, \gamma_i) = (\boldsymbol{x} - \boldsymbol{y}) \cdot \bar{\boldsymbol{n}}_i = \boldsymbol{x} \cdot \bar{\boldsymbol{n}}_i + \delta_i$$

The weighted sum of distances is given by

$$\begin{aligned}
\bar{h}(\boldsymbol{x}, \gamma_i) &= \sum_{i=1}^{n_f} \omega_i h^2(\boldsymbol{x}, \gamma_i) \\
&= \omega_i (\boldsymbol{x} \cdot \bar{\boldsymbol{n}}_i + \delta_i) \cdot (\boldsymbol{x} \cdot \bar{\boldsymbol{n}}_i + \delta_i) \\
&= \boldsymbol{x} \cdot \boldsymbol{A} \boldsymbol{x} + 2 \bar{\boldsymbol{b}} \cdot \boldsymbol{x} + c
\end{aligned}$$

where n_f is the number of facets connected to the vertex v_j, ω_i are the areas of these facets and

$$\boldsymbol{A} = \sum_{i=1}^{n_f} \omega_i \bar{\boldsymbol{n}}_i \otimes \bar{\boldsymbol{n}}_i \qquad \bar{\boldsymbol{b}} = \sum_{i=1}^{n_f} \omega_i \delta_i \bar{\boldsymbol{n}}_i \qquad c = \sum_{i=1}^{n_f} \omega_i \delta_i^2.$$

when this approach is used in the evaluation of the normals at a given vertex, we assume that all planes are moving by a unity, i.e. $\delta_i = 1$. The point $\boldsymbol{x}$ that minimizes the weighted sum of the squared distances to the

planes γ_i is given by the solution of the 3×3 linear system

$$\boldsymbol{A}\boldsymbol{x} = \bar{\boldsymbol{b}}. \tag{3}$$

The matrix $\boldsymbol{A}$ in Equation (3) is, in general, symmetric and positive semi-definite. Depending on the relative position of the facets, $\boldsymbol{A}$ can be nearly rank deficient, therefore it cannot always be solved using a standard linear solver. However, by performing an eigenvalue analysis of $\boldsymbol{A}$ one can effectively compute the intersection of the planes and estimate the normal at the vertex v_j.

Let $\lambda_1 \geq \lambda_2 \geq \lambda_3$ and $\bar{\boldsymbol{e}}_i$ be the eigenvalues and the corresponding orthonormal eigenvectors of $\boldsymbol{A}$, i.e. $\boldsymbol{A}\bar{\boldsymbol{e}}_i = \lambda_i \bar{\boldsymbol{e}}_i$ and $\boldsymbol{A} = \sum_{i=1}^{3} \lambda_i \bar{\boldsymbol{e}}_i \otimes \bar{\boldsymbol{e}}_i$. Given the eigenvalues and eigenvectors of $\boldsymbol{A}$, we define the *primary space* as the eigenvectors $\bar{\boldsymbol{e}}_i$ that have their corresponding eigenvalues $\lambda_i > \varepsilon \lambda_1$, where ε is a small number which can be computed relatively to the geometric representation of the surface. In practice, we choose ε to be 0.003. The complementary space corresponding to $\lambda_i < \varepsilon \lambda_1$ is called *null space*.

Using the *primary space* of the eigenvalues of $\boldsymbol{A}$, the estimate of the unit normal vector $\boldsymbol{n}_j$ at the vertex v_j can be defined as follows

$$\boldsymbol{n}_j = \frac{\boldsymbol{d}_j}{\|\boldsymbol{d}_j\|} \quad \text{where} \quad \boldsymbol{d}_j = \sum_{\{i|\lambda_i > \varepsilon \lambda_1\}} -\frac{\bar{\boldsymbol{e}}_i \cdot \bar{\boldsymbol{b}}}{\lambda_i}\bar{\boldsymbol{e}}_i$$

no summation on j indices.

(a) Distance to plane γ_i (b) Average tangent vector   (c) Projection tensor
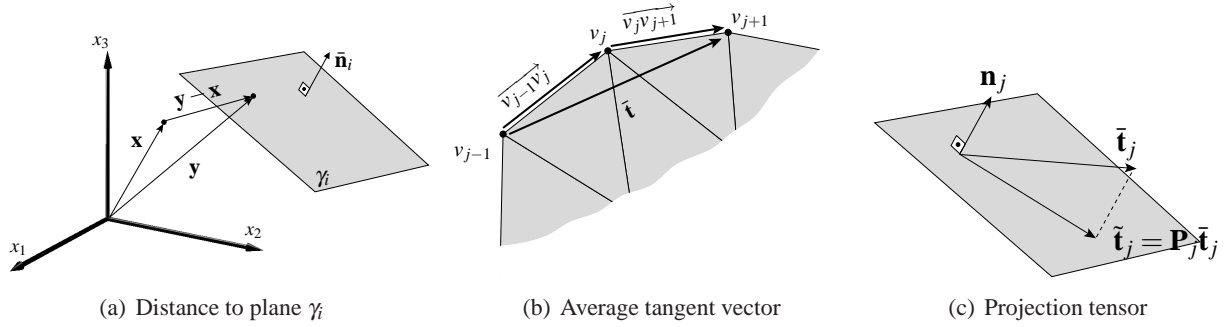
Figure 4: Steps for the evaluation of the normal, tangent and conormal vectors along the crack front.

Evaluation of the tangents   Given the normal at the vertex v_j, the evaluation of the tangents at the vertices along the crack front can be described in a two-step procedure.

First, we compute an estimate of the tangent vector by the sum of the vectors given by the two oriented segments formed by the vertex v_j and its neighbors along the crack front v_{j-1} and v_{j+1}

$$\bar{\boldsymbol{t}} = \overrightarrow{v_{j-1}v_j} + \overrightarrow{v_jv_{j+1}}.$$

Vectors $\overrightarrow{v_{j-1}v_j}$ and $\overrightarrow{v_jv_{j+1}}$ are illustrated in Figure 4(b). The orientation of these vectors is based on the sequence of the vertices along the front which, in turn, depends on the orientation of the facet normals.

The vector computed in the first step is, in general, not perpendicular to the vertex normal $\boldsymbol{n}_j$. Therefore, in the second step, we compute the vectorial component of $\bar{\boldsymbol{t}}$ that is perpendicular to $\boldsymbol{n}_j$ by applying the projection tensor $\boldsymbol{P}_j$ which is given by

$$\boldsymbol{P}_j = \boldsymbol{I} - \boldsymbol{n}_j \otimes \boldsymbol{n}_j.$$

The projection tensor procedure is illustrated in Figure 4(c). Thus, the unit tangent vector at the vertex v_j

can be written as follows

$$t_j = \frac{\tilde{t}_j}{\|\tilde{t}_j\|}$$

where $\tilde{t}_j = P_j \bar{t}_j$ and no summation implied in j indices.

Evaluation of the conormals   Once the normal and tangent are computed for a given vertex v_j, the conormal is simply the cross product between them.

$$b_j = n_j \times t_j$$

no summation implied in j indices.

4   Crack front approximation and enrichment functions

This section presents two approaches to build approximations to the crack front curvilinear coordinate system defined in Section 2. The computation of corresponding enrichment functions and their derivatives with respect to global coordinate directions is also presented. In the first approach, the curved crack front coordinate system is approximated by a set of Cartesian coordinate systems while in the second case a set of curvilinear (quadratic) approximations is used. *It should be noted that the shape and location of the crack front is dictated not only by the triangulation used to represent the crack surface but also by the coordinate systems used in the computation of the enrichment functions* (2). These *geometrical* approximations are denoted hereafter as *linear* and *quadratic* approximations of the crack front geometry. They should not be confused with the polynomial order of GFEM shape functions. In both approaches proposed here, each node x_α enriched with functions (2) defines its own coordinate system. Since the enrichment functions used at distinct clouds ω_α do not have to be the same, this does not pose any problem for the GFEM. The two procedures are presented in Sections 4.1 and 4.2, respectively.

A key ingredient of both procedures is the computation of unity vectors along the crack front that are normal to the crack surface, tangent to the crack front or oriented in the conormal (forward) direction of the crack front, as presented in Section 3.1.

4.1   Linear approximation of crack front geometry

In this approach, the crack front curvilinear coordinate system is approximated by a set of Cartesian coordinate systems. Each cloud ω_α enriched with functions (2) defines a rectangular coordinate system approximately tangent to the crack front as described below. Thus, the crack front shape is approximated by a set of linear segments.

The procedure to define the Cartesian coordinate system (ξ_1, ξ_2, ξ_3) used to compute enrichment functions (2) at a cloud ω_α associated with a finite element node x_α can be described as follows[1]

- Find the closest crack front vertex v_j to node x_α. This procedure can be efficiently implemented using geometric predicates.

- Compute at front vertex v_j unity vectors $\hat{e}_1, \hat{e}_2, \hat{e}_3$ oriented in the conormal direction to the crack front, normal direction to the crack surface and tangent direction to the crack front, respectively. The computation of these vectors is described in Section 3.1. They are taken as the base vectors of the coordinate system.

---

[1] A crack front vertex may be referenced using its index, v_j, or its coordinates, $\boldsymbol{v}_j$.

- Let v_{j-1} and v_{j+1} denote the index of the two crack front vertex nodes connected to vertex node v_j (cf. Figure 4(b)). The origin $\mathbf{O}$ of the coordinate system is taken as the average of the position vectors of these three crack front vertex nodes.

Figure 5 illustrates a crack front Cartesian coordinate system (ξ_1, ξ_2, ξ_3) built as described above. A straight cylindrical coordinate system (r, θ, ξ_3) can be defined using (ξ_1, ξ_2, ξ_3), as described below. This system is used in the computation of the singular enrichments (2). Thus, these functions represent a locally straight crack front in the cloud ω_α. Since clouds along crack fronts are very small due to mesh refinement, this approximation of a curved crack front is acceptable. Numerical experiments presented in Section 5 confirm this hypothesis.
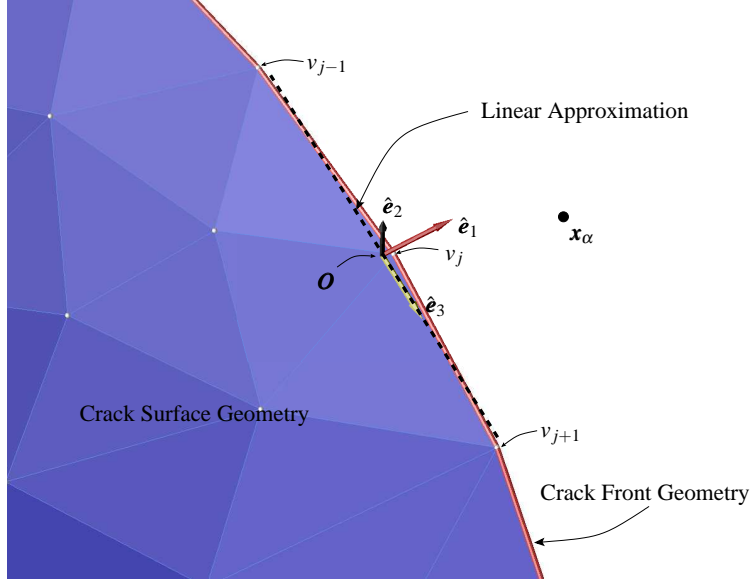

Figure 5: Base vectors and origin of a Cartesian coordinate system used for the computation of enrichment functions for node $\mathbf{x}_\alpha$. Each node with singular enrichment defines its own Cartesian coordinate system. As a result, the crack front shape is approximated by a set of linear segments.

4.1.1 Transformation of enrichment functions to global coordinates

Enrichment functions $\bar{L}_{\alpha i}^{\xi_j}(r, \theta)$, $i = 1, 2$, $j = 1, 2, 3$, computed in the cylindrical coordinate system are transformed to the global Cartesian system (X_1, X_2, X_3) as follows.

Define

$$\hat{L}_{\alpha i}^{\xi_j}(\xi_1, \xi_2, \xi_3) = \bar{L}_{\alpha i}^{\xi_j} \circ T_a^{-1}(\xi_1, \xi_2, \xi_3) \qquad i = 1, 2, \; j = 1, 2, 3 \tag{4}$$

where "$\circ$" denotes composition of two functions. The transformation

$$T_a^{-1} : (\xi_1, \xi_2, \xi_3) \longmapsto (r, \theta, \xi_3)$$

is given by

$$\left\{ \begin{array}{c} r \\ \theta \\ \xi_3 \end{array} \right\} = \left\{ \begin{array}{c} \sqrt{\xi_1^2 + \xi_2^2} \\ \arctan(\dfrac{\xi_2}{\xi_1}) \\ \xi_3 \end{array} \right\} \tag{5}$$

9

The Jacobian of this transformation is given by

$$\left[\left(\boldsymbol{J}_a^{-1} \right)_{ij} \right] = \left[\frac{\partial r_i}{\partial \xi_j} \right] = \begin{bmatrix} \cos(\theta) & \sin(\theta) & 0 \\ -\frac{1}{r}\sin(\theta) & \frac{1}{r}\cos(\theta) & 0 \\ 0 & 0 & 1 \end{bmatrix} \tag{6}$$

where r_i, $i = 1, 2, 3$, denote cylindrical coordinates r, θ and ξ_3, respectively.

Next define

$$\tilde{L}_{\alpha i}^{\xi_j}(X_1, X_2, X_3) = \hat{L}_{\alpha i}^{\xi_j} \circ T_b^{-1}(X_1, X_2, X_3) \qquad i = 1, 2, \; j = 1, 2, 3 \tag{7}$$

where the transformation

$$T_b^{-1} : (X_1, X_2, X_3) \longmapsto (\xi_1, \xi_2, \xi_3)$$

is given by

$$\left\{ \begin{array}{c} \xi_1 \\ \xi_2 \\ \xi_3 \end{array} \right\} = \boldsymbol{R}_b^{-1} \left\{ \begin{array}{c} X_1 - O_1 \\ X_2 - O_2 \\ X_3 - O_3 \end{array} \right\} \tag{8}$$

Above, (O_1, O_2, O_3) are the coordinates of the origin $\boldsymbol{O}$ of the crack coordinate system and $\boldsymbol{R}_b^{-1} \in \mathfrak{R}^3 \times \mathfrak{R}^3$ is a rotation matrix with rows given by the base vectors $\hat{\boldsymbol{e}}_i$, $i = 1, 2, 3$.

The Jacobian of this transformation is given by

$$\left(\boldsymbol{J}_b^{-1} \right)_{ij} = \frac{\partial \xi_i}{\partial X_j} = \left(\boldsymbol{R}_b^{-1} \right)_{ij}$$

The displacement vectors $(\tilde{L}_{\alpha 1}^{\xi_1}, \tilde{L}_{\alpha 1}^{\xi_2}, \tilde{L}_{\alpha 1}^{\xi_3})$ and $(\tilde{L}_{\alpha 2}^{\xi_1}, \tilde{L}_{\alpha 2}^{\xi_2}, \tilde{L}_{\alpha 2}^{\xi_3})$ have components in the crack front coordinate directions ξ_1, ξ_2, ξ_3 and thus must be transformed to the global Cartesian system (X_1, X_2, X_3) using

$$\left\{ \begin{array}{cc} L_{\alpha 1}^{X_1} & L_{\alpha 2}^{X_1} \\ L_{\alpha 1}^{X_2} & L_{\alpha 2}^{X_2} \\ L_{\alpha 1}^{X_3} & L_{\alpha 2}^{X_2} \end{array} \right\} = \boldsymbol{R}_b \left\{ \begin{array}{cc} \tilde{L}_{\alpha 1}^{\xi_1} & \tilde{L}_{\alpha 2}^{\xi_1} \\ \tilde{L}_{\alpha 1}^{\xi_2} & \tilde{L}_{\alpha 2}^{\xi_2} \\ \tilde{L}_{\alpha 1}^{\xi_3} & \tilde{L}_{\alpha 2}^{\xi_3} \end{array} \right\} \tag{9}$$

where $\boldsymbol{R}_b = (\boldsymbol{R}_b^{-1})^T$. Functions $L_{\alpha i}^{X_j}$, $i = 1, 2$, $j = 1, 2, 3$, can now be used in (1) to define GFEM shape functions. The computation of their derivatives with respect to global coordinate directions is presented in Appendix A. These functions are the same as those in Equation (11) of [28]. They are also presented in Section 4 of [4].

4.2 Quadratic approximation of crack front geometry

This section presents another approximation for the curvilinear crack front coordinate system described in Section 2. Here, each cloud ω_α uses a quadratic approximation of the crack front geometry. Three crack front vertices are used to fit a quadratic curve to the crack front as illustrated in Figure 6. This quadratic curve corresponds to the coordinate line ξ_3 of the curvilinear coordinate system (ξ_1, ξ_2, ξ_3) shown in Figure 1. As before, this system is used for the construction of singular enrichment functions used at nodes near the crack front. The key idea in defining this system is to use a 12-node hexahedral element along the crack front. The coordinate lines of the curved hexahedron are used in the definition of the coordinate lines of the crack front coordinate system. A hexahedral coordinate line ξ_3 in physical coordinates defines a quadratic approximation of the crack front shape. Figure 6 illustrates the idea. In this approach, both

10

the crack front and the crack surface can be curved. The only assumption we make regarding the shape of the crack surface is that, *within a cloud* ω_α, the surface is flat in the crack front conormal direction ξ_1. Transformation of coordinates between this system and the global coordinate system (X_1, X_2, X_3) is then defined using the shape functions and nodal coordinates of the hexahedral element. The construction of the curved hexahedron can be fully automated without difficulty. It should be noted the 12-node hexahedra are *used only to define curvilinear coordinate systems*. They do not add any degrees of freedom to the problem. Details are presented below.

In this section, ξ_1, ξ_2 and ξ_3 may denote either a coordinate in the master coordinate system of a brick or the corresponding coordinate line in physical space (X_1, X_2, X_3). The meaning is clear from the context.
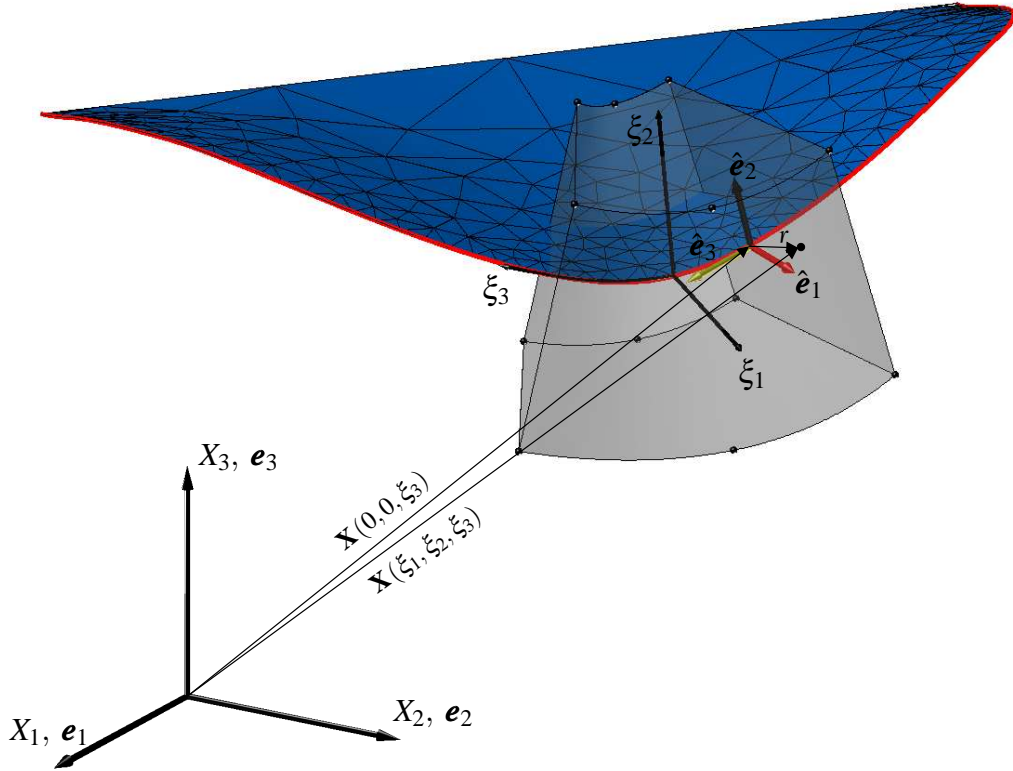

Figure 6: Non-planar crack surface and coordinate system for curved front enrichment.

4.2.1 Construction of hexahedra along a curved crack front

For each cloud ω_α enriched with singular functions, a 12-node hexahedral element is defined along the crack front using the following procedure.

1. Let $\boldsymbol{x}_\alpha$ denote the finite element node associated with cloud ω_α. Find the closest crack front vertex v_j to node $\boldsymbol{x}_\alpha$. This procedure can be efficiently implemented using geometric predicates. This step is illustrated in Figure 7(a).

2. The dimensions of the hexahedral element are set such that it contains the cloud ω_α, the support of the enrichment functions used at node $\boldsymbol{x}_\alpha$. Let h_α denote the radius of the smallest sphere with origin at $\boldsymbol{x}_\alpha$ that contains ω_α. Since the origin of the hexahedral is, in general, not equal to $\boldsymbol{x}_\alpha$, we request

11

that the hexahedral contains a sphere of radius given by

$$r_{\text{sphere}} = \| \overrightarrow{\boldsymbol{v}_j \boldsymbol{x}_\alpha} \| + h_\alpha$$

where $\| \overrightarrow{\boldsymbol{v}_j \boldsymbol{x}_\alpha} \|$ is the distance from the closest crack front vertex, $\boldsymbol{v}_j$, to the finite element node $\boldsymbol{x}_\alpha$. This step is illustrated in Figure 7(b).

3. Define the dimension, l_h, of the edges of the hexahedral cross-section at $\xi_3 = -1.0$, $\xi_3 = 0.0$, and $\xi_3 = 1.0$. The hexahedral cross-section is squared and l_h is taken as $l_h = 2r_{\text{sphere}}$.

4. Starting from vertex v_j, select the two closest vertices, $v_{\text{j, right}}$ and $v_{\text{j, left}}$, along the crack front directions $\xi_3 = 1$ and $\xi_3 = -1$, respectively, such that they are located outside of the sphere with radius r_{sphere} and origin $\boldsymbol{v}_j$. This step is illustrated in Figure 7(c).

5. Compute at front vertices $v_{\text{j, left}}$, v_j and $v_{\text{j, right}}$ the triad $\boldsymbol{b}$, $\boldsymbol{n}$, $\boldsymbol{t}$ oriented in the conormal direction of the crack front, normal to the crack surface and tangent to the crack front, respectively. The computation of these vectors is described in Section 3.1. Crack front vertices coordinates $\boldsymbol{v}_{\text{j, left}}$, $\boldsymbol{v}_j$ and $\boldsymbol{v}_{\text{j, right}}$ and the triads are then used to define the coordinates of the element nodes. For example, the squared face $\xi_3 = 1$ with edge length l_h contains $\boldsymbol{v}_{\text{j, right}}$ and is normal to the tangent vector computed at $\boldsymbol{v}_{\text{j, right}}$. The face edges are either in the direction $\boldsymbol{n}$ or $\boldsymbol{b}$. This step is illustrated in Figure 7(d) which shows a 12-node hexahedron built using the procedure described above.

A curvilinear cylindrical coordinate system (r, θ, ξ_3) along the crack front can be defined using brick coordinates (ξ_1, ξ_2, ξ_3), as described below. This system is used in the computation of the singular enrichment functions (2). These computations involve transformations of vectors and their derivatives between coordinate systems (X_1, X_2, X_3), (ξ_1, ξ_2, ξ_3) and (r, θ, ξ_3). Details on this are provided below.

4.2.2 Transformation map between global (Cartesian) coordinates and curvilinear coordinates at the crack front

In this section, we present the coordinate transformations between the global Cartesian system (X_1, X_2, X_3) and the curvilinear crack front coordinate systems (ξ_1, ξ_2, ξ_3) and (r, θ, ξ_3). These transformations are used to define enrichment functions $\bar{L}_{\alpha i}^{\xi_j}(r, \theta)$, $i = 1, 2$, $j = 1, 2, 3$, in the global coordinate system. Transformation of derivatives of these functions is presented in Appendix A.

T_1 **- Transformation between coordinate systems** (X_1, X_2, X_3) **and** (ξ_1, ξ_2, ξ_3) Once the hexahedron that defines the curvilinear coordinates (ξ_1, ξ_2, ξ_3) along the crack front has been built, unitary base vectors for this system and the transformation between this system and the global Cartesian system (X_1, X_2, X_3) can be computed as described below.
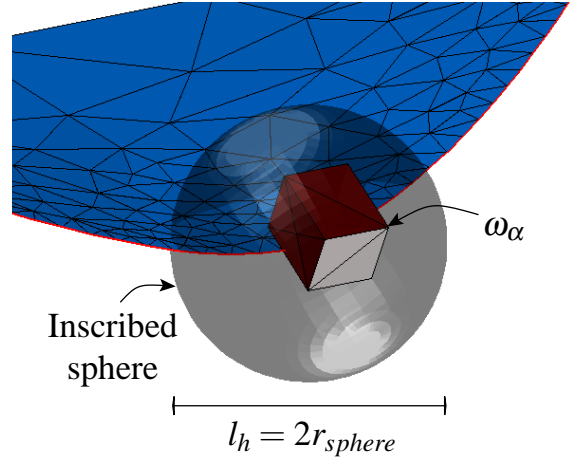
The transformation from master coordinates (ξ_1, ξ_2, ξ_3) to global coordinates (X_1, X_2, X_3) is defined by

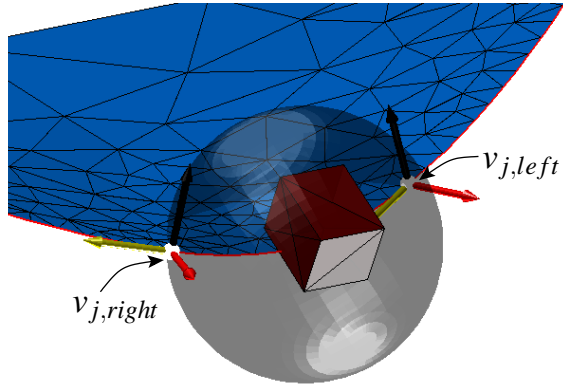$$T_1 : (\xi_1, \xi_2, \xi_3) \longmapsto (X_1, X_2, X_3)$$

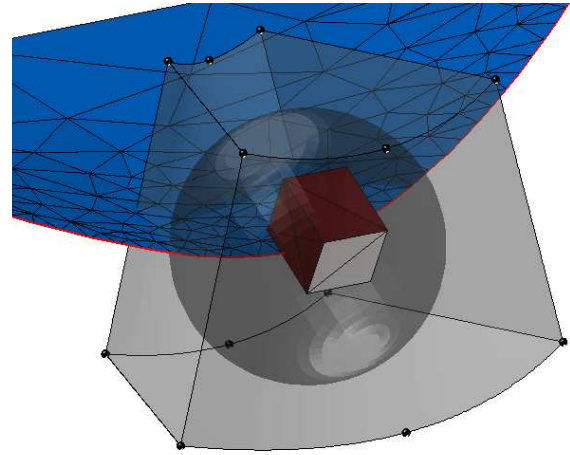$$X_i(\xi_1, \xi_2, \xi_3) = \sum_{j=1}^{12} X_{ij} N_j(\xi_1, \xi_2, \xi_3)$$
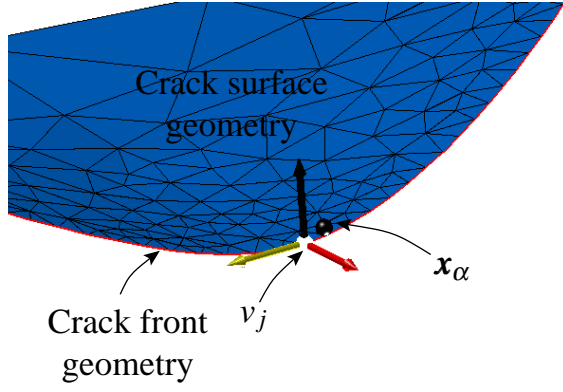
(a) Step 1: Selection of the closest crack front vertex v_j to enriched node x_α.

(b) Steps 2 and 3: Define inscribed sphere and dimension of element edges at faces $\xi_3 = -1.0$, $\xi_3 = 1.0$.

(c) Step 4: Find neighboring vertices $v_{j, right}$ and $v_{j, left}$ to v_j along the crack front.

(d) Step 5: Define nodal coordinates for curved hexahedron.

Figure 7: Steps for the construction of a hexahedron element that defines a curvilinear coordinate system used for the computation of singular enrichment functions at cloud ω_α. The pictures presented here are based on actual data from a GFEM mesh and crack surface triangulation. The cloud ω_α shown in the figures is the union of the set of tetrahedral elements that share the node x_α.
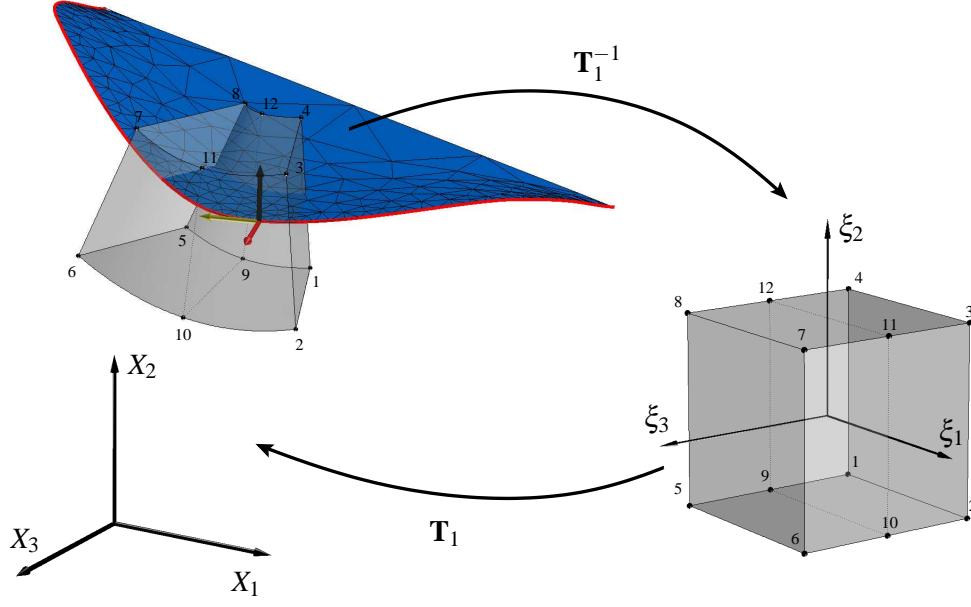
Figure 8: Transformation map T_1.

where the shape functions $N_j(\xi_1, \xi_2, \xi_3)$ are given by

$$
\begin{aligned}
N_1(\xi_1, \xi_2, \xi_3) &= 1/8(1-\xi_1)(1-\xi_2)(\xi_3^2 - \xi_3) \\
N_2(\xi_1, \xi_2, \xi_3) &= 1/8(1+\xi_1)(1-\xi_2)(\xi_3^2 - \xi_3) \\
N_3(\xi_1, \xi_2, \xi_3) &= 1/8(1+\xi_1)(1+\xi_2)(\xi_3^2 - \xi_3) \\
N_4(\xi_1, \xi_2, \xi_3) &= 1/8(1-\xi_1)(1+\xi_2)(\xi_3^2 - \xi_3) \\
N_5(\xi_1, \xi_2, \xi_3) &= 1/8(1-\xi_1)(1-\xi_2)(\xi_3^2 + \xi_3) \\
N_6(\xi_1, \xi_2, \xi_3) &= 1/8(1+\xi_1)(1-\xi_2)(\xi_3^2 + \xi_3) \\
N_7(\xi_1, \xi_2, \xi_3) &= 1/8(1+\xi_1)(1+\xi_2)(\xi_3^2 + \xi_3) \\
N_8(\xi_1, \xi_2, \xi_3) &= 1/8(1-\xi_1)(1+\xi_2)(\xi_3^2 + \xi_3) \\
N_9(\xi_1, \xi_2, \xi_3) &= 1/4(1-\xi_1)(1-\xi_2)(1-\xi_3^2) \\
N_{10}(\xi_1, \xi_2, \xi_3) &= 1/4(1+\xi_1)(1-\xi_2)(1-\xi_3^2) \\
N_{11}(\xi_1, \xi_2, \xi_3) &= 1/4(1+\xi_1)(1+\xi_2)(1-\xi_3^2) \\
N_{12}(\xi_1, \xi_2, \xi_3) &= 1/4(1-\xi_1)(1+\xi_2)(1-\xi_3^2)
\end{aligned}
$$

and X_{ij} are the nodal coordinates for the curved hexahedron defined in Section 4.2.1. This transformation and its inverse are illustrated in Figure 8. Note that the master coordinates (ξ_1, ξ_2, ξ_3) define *coordinate lines* along the curvilinear crack front as discussed earlier. These coordinates lines are illustrated in Figure 6.

14

The Jacobian for this transformation is given by

$$\left[(J_1)_{ij} = \frac{\partial X_i}{\partial \xi_j} \right] = \begin{bmatrix} \dfrac{\partial X_1}{\partial \xi_1} & \dfrac{\partial X_1}{\partial \xi_2} & \dfrac{\partial X_1}{\partial \xi_3} \\ \dfrac{\partial X_2}{\partial \xi_1} & \dfrac{\partial X_2}{\partial \xi_2} & \dfrac{\partial X_2}{\partial \xi_3} \\ \dfrac{\partial X_3}{\partial \xi_1} & \dfrac{\partial X_3}{\partial \xi_2} & \dfrac{\partial X_3}{\partial \xi_3} \end{bmatrix} \tag{10}$$

The columns of J_1 define vectors tangent to the coordinate lines in physical coordinates and are given by

$$\hat{g}_j = \frac{\partial X}{\partial \xi_j} = \frac{\partial X_i}{\partial \xi_j} e_i \tag{11}$$

where e_i is a base vector of the global coordinate system. Unitary base vectors along the crack front are then given by

$$\hat{e}_j = \frac{\hat{g}_j}{\hat{h}_j} \qquad \text{(no summation on } j) \tag{12}$$

where the *scale factor* $\hat{h}_j$ is given by

$$\hat{h}_j = \sqrt{\hat{G}_{jj}} \qquad \text{(no summation on } j) \tag{13}$$

and $\hat{G}$ is the metric tensor defined as

$$\hat{G}_{ij} = \hat{g}_i \cdot \hat{g}_j \tag{14}$$

The base vectors $\hat{e}_j$, $j = 1, 2, 3$ are the red, black and yellow arrows illustrated in Figure 6. Since the coordinate lines ξ_1 and ξ_2 are not curvilinear, the base vectors $\hat{e}_j$, $j = 1, 2, 3$, and the other quantities defined above are a function of ξ_3 only. This simplifies the calculations as shown in Appendix A.

The inverse mapping

$$T_1^{-1} : (X_1, X_2, X_3) \longmapsto (\xi_1, \xi_2, \xi_3)$$

is needed for the computational implementation of the enrichment functions as discussed in Section 4.2.2. It can be numerically determined using an iterative scheme such as Newton-Raphson.

After performing the inverse mapping, the closest point on the curved front to X is given by $X(0, 0, \xi_3)$. Thus, the distance of X to the crack front is given by

$$r(X) = \| X - X(0, 0, \xi_3) \| \tag{15}$$

This is used below to define the curvilinear cylindrical coordinate system needed for the computation of singular enrichment functions (2).

Curvilinear cylindrical coordinate system along crack front Having coordinates (ξ_1, ξ_2, ξ_3) computed using mapping T_1^{-1}, a curvilinear cylindrical coordinate system along the crack front can be defined through the following transformation

$$T_2^{-1} : (\xi_1, \xi_2, \xi_3) \longmapsto (r, \theta, \xi_3)$$

with the relation between coordinates in both systems given by

$$
\begin{cases}
r = \| \boldsymbol{X}(\xi_1, \xi_2, \xi_3) - \boldsymbol{X}(0, 0, \xi_3) \| \\
\theta = \arctan(\dfrac{\xi_2}{\xi_1})
\end{cases}
\tag{16}
$$

The Jacobian for this transformation is given by

$$
\boldsymbol{J}_2^{-1} =
\begin{bmatrix}
\cos(\theta) & \sin(\theta) & 0 \\
-\dfrac{1}{r}\sin(\theta) & \dfrac{1}{r}\cos(\theta) & 0 \\
0 & 0 & 1
\end{bmatrix}
\tag{17}
$$

which is equal to $\boldsymbol{J}_a^{-1}$ defined in (6).

Definition of enrichment functions in global coordinates Transformations T_1^{-1} and T_2^{-1} can be used to define enrichment functions $\bar{L}_{\alpha i}^{\xi_j}(r, \theta)$, $i = 1, 2$, $j = 1, 2, 3$, in global coordinates.

Define

$$
\hat{L}_{\alpha i}^{\xi_j}(\xi_1, \xi_2, \xi_3) = \bar{L}_{\alpha i}^{\xi_j} \circ T_2^{-1}(\xi_1, \xi_2, \xi_3) \qquad i = 1, 2, \ j = 1, 2, 3
\tag{18}
$$

Next define

$$
\tilde{L}_{\alpha i}^{\xi_j}(X_1, X_2, X_3) = \hat{L}_{\alpha i}^{\xi_j} \circ T_1^{-1}(X_1, X_2, X_3) \qquad i = 1, 2, \ j = 1, 2, 3
\tag{19}
$$

In the computational implementation of the singular enrichment functions, an integration point in the support ω_α of these functions is first mapped to global coordinates $\boldsymbol{X}$ and then mapped to cylindrical coordinates using the composition of T_1^{-1} and T_2^{-1}, i.e.,

$$
T^{-1} = T_2^{-1} \circ T_1^{-1}
$$

where

$$
T^{-1} : (X_1, X_2, X_3) \longmapsto (r, \theta, \xi_3)
$$

Mapped coordinates (r, θ, ξ_3) are then used in (2) to compute the singular functions.

The displacement vectors $(\tilde{L}_{\alpha 1}^{\xi_1}, \tilde{L}_{\alpha 1}^{\xi_2}, \tilde{L}_{\alpha 1}^{\xi_3})$ and $(\tilde{L}_{\alpha 2}^{\xi_1}, \tilde{L}_{\alpha 2}^{\xi_2}, \tilde{L}_{\alpha 2}^{\xi_3})$ have components in the crack front coordinate directions ξ_1, ξ_2, ξ_3 and thus must be transformed to the global Cartesian system (X_1, X_2, X_3) using the same procedure as in Section 4.1.1. This can be done using (9) with $\boldsymbol{R}_b$ replaced by $\boldsymbol{R}_1$, a rotation matrix with columns given by the base vectors $\hat{\boldsymbol{e}}_i$, $i = 1, 2, 3$, defined in (12).

5   Numerical experiments

In the numerical examples presented in this paper, crack front enrichment functions are used at nodes whose support intersects the crack front. More details about the selection of nodal GFEM enrichments in 3D fracture mechanics problems can be found in, e.g, [28].

We use the Cut-off Function Method (CFM) to extract stress intensity factors from GFEM solutions. The CFM is a superconvergent extraction technique based on Betti's reciprocity law. It is able to deliver convergence rates for SIFs that are on par with the convergence rate of strain energy. More details about this extraction method can be found in, e.g, [26, 27, 36, 37].

5.1 Half penny-shaped crack in a prism

In this example, we consider a half penny-shaped crack in a prism as illustrated in Figure 9. The ratio of the characteristic dimension, L, of the prism and the radius a of the crack is $L/a = 5.0$. The prism is subjected to top and bottom tensile tractions of magnitude $\sigma = 1$. Figure 9 illustrates the boundary conditions and the dimension of the domain of analysis. The Young's Modulus and Poisson's ratio are taken as $E = 1.0$ and $v = 0.25$, respectively.

The reference solution for stress intensity factor (SIF) in this problem is provided by [39]. There, one quarter of the domain was discretized with hex-20 finite elements and appropriate symmetry boundary conditions applied. The localized mesh refinement around the crack front consisted of a set of seven rings of elements. Hexagonal 20-node elements with quarter-point nodes and collapsed faces were used along the crack front. The ratio element size to characteristic crack length (L_e/a) was 3.83×10^{-3} [39]. This is around ten times smaller than the finest mesh we use (cf. Table 1).

The SIF solutions (K_I) obtained in this section are normalized by the equation

$$\bar{K}_I = \frac{K_I}{\sigma\sqrt{\dfrac{\pi a}{Q}}}$$

where $Q = 2.464$ for a circular crack. More details about this normalization process can be found in [39] and references therein.

The aim of this example is to show a comparison for SIF solution between linear and quadratic crack front geometry approximations for different mesh refinements at the crack front. Since this example has a surface breaking crack, the boundary layer effect [29] reduces the SIF values when the crack front is close to the boundary of the domain. Because the boundary layer effect is not the main focus of this paper, we compute the SIF in the range $10° \leq \theta \leq 170°$.

We use three GFEM meshes with different levels of refinement along the crack front and polynomial order of approximation $p = 3$. More details about high-order GFEM approximations for the class of problems considered here can be found in [28]. The description of each mesh according to its level of refinement is listed in Table 1. Figure 9 illustrates the refinement along the crack front for the three meshes used in this analysis. Mesh 1 is the coarsest mesh that allows the construction of the 12-node hexahedron under the assumptions listed in Section 4.2.1.

Table 1: Description of GFEM meshes used in the simulation. The ratios L_e/a listed below refer to the elements that intersect the crack front.

Mesh	dofs	L_e/a min	L_e/a max
1	15132	0.1250	0.3125
2	33102	0.0625	0.1180
3	82590	0.0294	0.0525

The use of coarse meshes around the crack front brings the issue of numerical integration of the singular enrichments. In [25], we show that the Keast integration rule [12] with 45 points is able to numerically integrate with sufficient accuracy these functions on meshes with element size typically used in the GFEM. Mesh 3 fits in this category but meshes 1 and 2 do not. In this example, we use a tensor product rule with 343 points in order to control integration errors. The same rule is used on all three meshes.
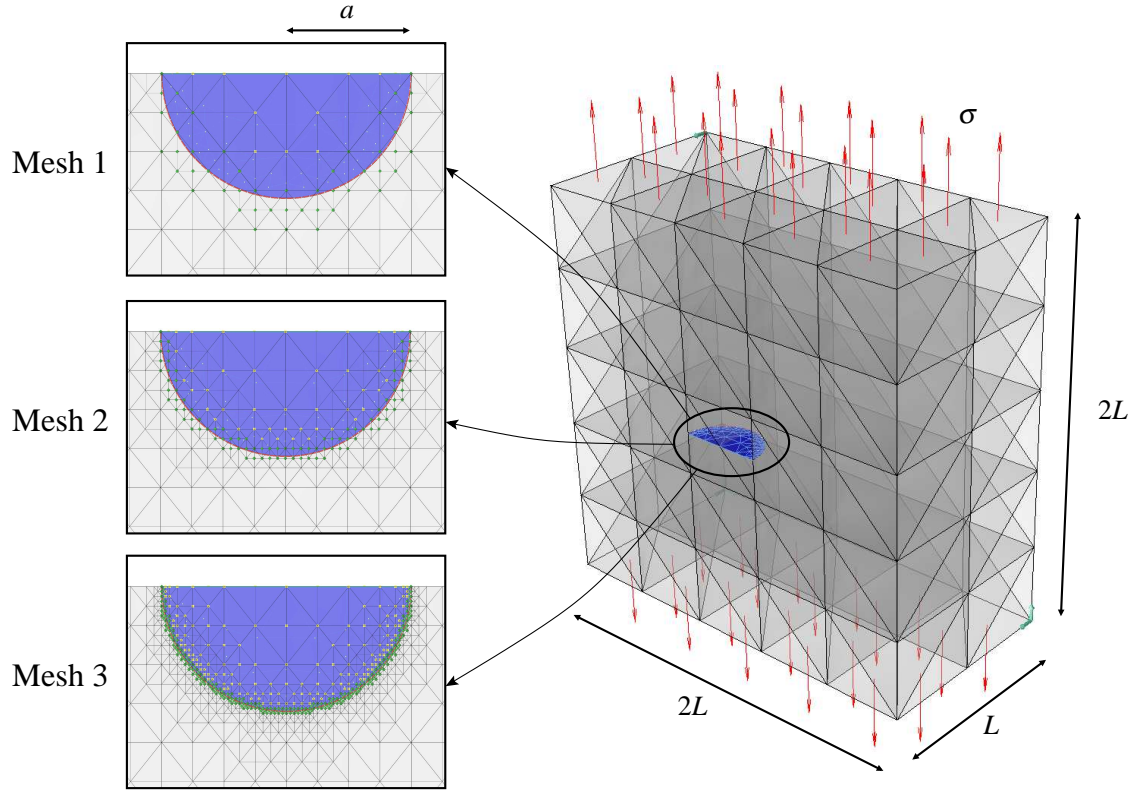
Figure 9: Half penny-shaped crack in a prism subjected to top and bottom uniform tractions: Initial coarse mesh with boundary conditions and crack surface representation. Zoom in shows the three meshes around the crack front (left). Green glyphs represent Westergaard enrichment with either straight (Section 4.1) or curved (Section 4.2) crack front geometry approximation. Yellow glyphs represent high-order step functions [28].

Figures 10(a), 10(b), and 10(c) illustrate the performance of linear and quadratic crack front geometry approximations on GFEM meshes 1, 2, and 3, respectively. Table 2 lists the minimum, maximum, average, and standard deviation of the relative difference between GFEM and FEM solutions along half of the crack front. One can observe that solutions computed with either crack front approximations show very oscillatory behavior and high error values for Mesh 1. The oscillations are gradually smoothed out as the level of crack front refinement increases. In the case of Mesh 3, the GFEM solutions are virtually identical and in good agreement with the reference solution. Figure 10(d) shows the SIF solution for the entire crack front. We can see that both crack front enrichments show symmetry with respect to the middle of the crack front. These results illustrate the robustness of both crack front descriptions. Moreover, the results for Mesh 3 show good agreement with the reference solution. The average error for the linear crack front geometry approximation is around -0.024% with standard deviation of about 0.21%.

(a) Normalized SIF along half of crack front for Mesh 1.

(b) Normalized SIF along half of crack front for Mesh 2.

(c) Normalized SIF along half of crack front for Mesh 3.

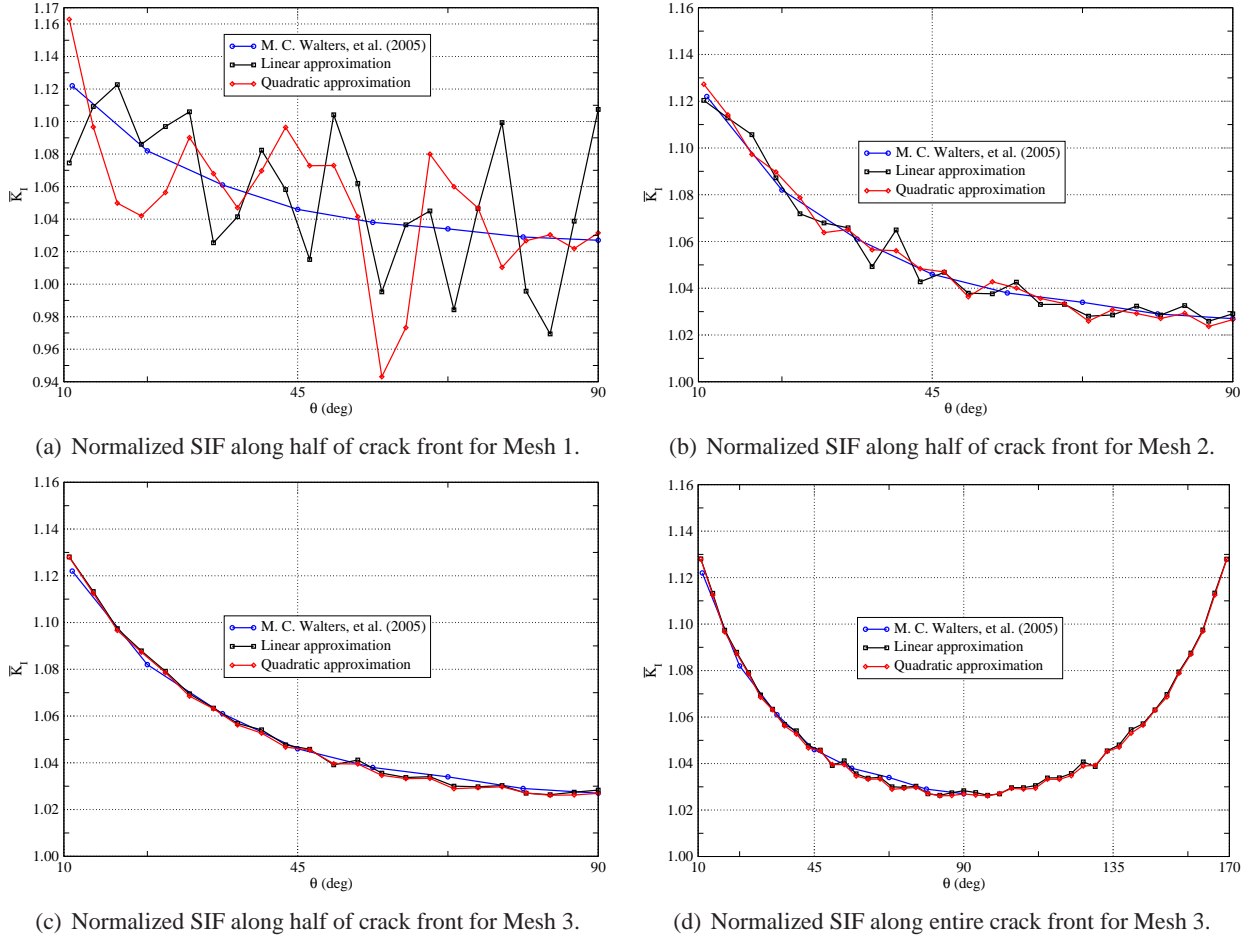(d) Normalized SIF along entire crack front for Mesh 3.

Figure 10: Normalized stress intensity factors (SIF) along the crack front for various meshes.

5.1.1 Convergence Analysis

This section presents convergence analyses of linear and quadratic crack front approximations. Two cases are considered. In the first one, GFEM meshes 1, 2 and 3 (cf. Table 1) are used while the crack surface representation is kept fixed. In the second case, GFEM Mesh 3 is used with three crack surface triangulations. In this case, the analysis starts with the coarsest crack front description that allows the construction of the

Table 2: Relative error, $|K_I - \hat{K}_I|/\hat{K}_I$, of SIF for GFEM meshes 1, 2 and 3. The reference values for the stress intensity factor, $\hat{K}_I$, are provided by the FEM solution of Walters et al. [39].

Mesh	Crack front geom. approximation	abs(min)	abs(max)	Error % average	std. deviation
1	Linear	0.0547	7.8435	-0.3553	3.7107
	Quadratic	0.1638	9.1141	0.1153	3.3504
2	Linear	0.0427	1.2096	-0.0224	0.4639
	Quadratic	0.0006	0.6584	-0.0197	0.3138
3	Linear	0.0101	0.4187	-0.0242	0.2083
	Quadratic	0.0040	0.3694	0.0396	0.2027

hexahedral for quadratic crack front approximation (cf. Section 4.2.1). The crack front segment length for this mesh is denoted by d. The length of the crack front segments in the subsequent crack surface meshes are $d/2$ and $d/3$ and they are constant along the crack front. These crack surface meshes are referred to as crack meshes d_1, d_2 and d_3, respectively.

In order to quantify the error of the stress intensity factor solution along the crack front, we use a normalized L^2-norm of the difference between the GFEM and the reference FEM solution defined by

$$e^r(K_i) := \frac{\|e_i\|_{L^2}}{\|\hat{K}_i\|_{L^2}} = \frac{\sqrt{\sum_{j=1}^{N_{ext}} \left(K_i^j - \hat{K}_i^j\right)^2}}{\sqrt{\sum_{j=1}^{N_{ext}} \left(\hat{K}_i^j\right)^2}} \tag{20}$$

where N_{ext} is the number of extraction points along the crack front, $\hat{K}_i^j$ and K_i^j are the reference and GFEM stress intensity factor values for mode i at the crack front point j, respectively. Hereafter, the quantity $e^r(K_i)$ is referred to as a normalized *error* even though the reference FEM solution is not the exact solution of the problem.

Figure 11 illustrates the convergence of the relative error $e^r(K_I)$ of the stress intensity factor K_I along the crack front using GFEM meshes 1, 2 and 3 and a fixed crack mesh. For reference, the convergence rate in strain energy for a finite element solution using uniform mesh refinement is $\beta \simeq 0.32$ [36]. One can observe that linear and quadratic approximations show similar convergence behavior when applying localized refinement of the GFEM mesh along the crack front. The quadratic approximation shows slightly faster convergence rate in the pre-asymptotic range. Nonetheless, both approximations converge to very close normalized L^2-norm values when a more refined GFEM mesh is used.

Table 3 lists the results of the second convergence study described above. It shows the relative error $e^r(K_I)$ of the stress intensity factor K_I along the crack front corresponding to GFEM mesh 3 and crack surface meshes d_1, d_2 and d_3. In order to provide consistent values for $e^r(K_I)$, the stress intensity factor along the crack front is computed at the same locations in all crack surface meshes, regardless of the level of refinement of the crack front geometry. Linear and quadratic crack front approximations present virtually equal convergence behavior with respect to the refinement of the crack front geometry. Crack Mesh d_1 shows larger error values than crack meshes d_2 and d_3. The computed relative error $e^r(K_I)$ levels off with refinement of the crack front representation, as expected. Further reduction of the error requires a finner or
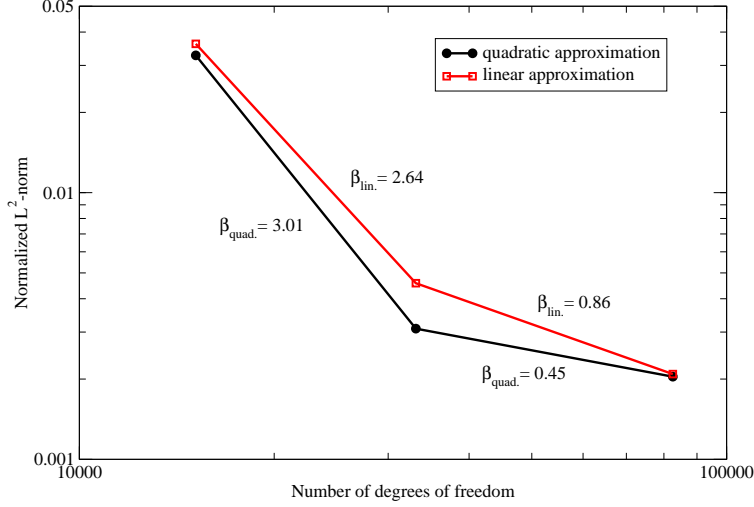
Figure 11: Relative error $e^r(K_I)$ of the stress intensity factor K_I along the crack front for linear and quadratic crack front approximations. $\beta_{\text{lin.}}$ and $\beta_{\text{quad.}}$ denote the convergence rate for linear and quadratic approximations, respectively. GFEM meshes 1, 2 and 3 and a fixed crack mesh are used in the computations.

higher order GFEM mesh.

Table 3: Convergence analysis of GFEM solution with respect to the refinement of the crack front description for linear and quadratic crack front approximations.

		$e^r(K_I)$	
Mesh	Front segment	linear	quadratic
d_1	$d = 0.0283$	0.003754	0.003832
d_2	$d/2 = 0.0143$	0.001794	0.001740
d_3	$d/3 = 0.0095$	0.001621	0.001638

5.2 Inner and outer circumferential cracks in a finite cylinder

In this section, we consider two examples of cracks in a finite cylinder. The cylinder has dimensions $L/R = 4$, where $2L$ is the height of the cylinder and R is the radius of its cross section. We set a large ratio between height and radius of the cylinder in order to minimize the finite domain effect in the extraction of stress intensity factors. The model is subjected to unit tensile load $\sigma = 1$ on top and bottom faces. $E = 1$ and $v = 0.3$ are the material parameters assigned to the cylinder. The first example is a penny-shaped crack, hereafter referred to as *inner crack*, in the middle of the cylinder. For this example $R/a = 5$, where a is the radius of the crack. The second example is a circumferential surface breaking crack, from now on referred to as *outer crack*, in the middle of the cylinder. In this case, a defines the material ligament. The ratio of the radius of the cylinder (R) to the crack length (c) is $R/c = 1.25$. The ratios cylinder radius to crack size, R/a and R/c, are set such that the inner and outer crack front geometries are the same. Figure 12 illustrates the domain of analysis and the crack surfaces used in the simulations.

The main objective of these examples is to compare the robustness of the crack front enrichment functions in cases where the curved crack front is convex (inner crack) and concave (outer crack). As reference
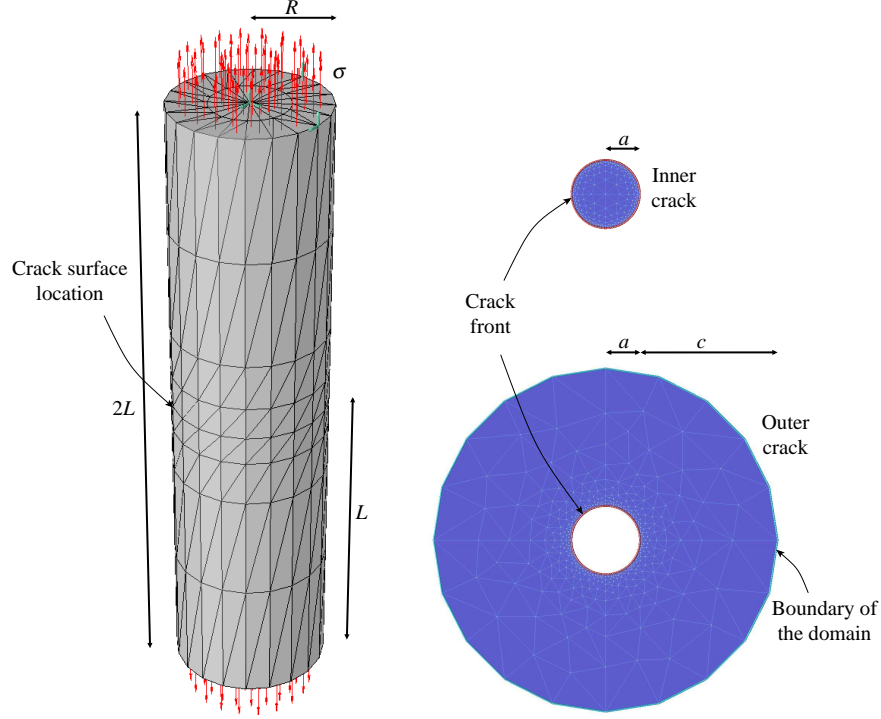
Figure 12: Finite cylinder subjected to top and bottom uniform tensile tractions and crack surface representation for outer and inner cracks.

solutions, we use the reference SIF solution for an infinite cylinder with a penny-shaped crack provided by [38]

$$\overset{\infty\,in}{K_I} = 1.008\sigma\sqrt{\pi a}$$

and the solution for a circumferential external crack in a infinite cylinder provided by [21]

$$\overset{\infty\,out}{K_I} = 6.115\sigma\sqrt{\pi c}.$$

According to the references, the accuracy for $\overset{\infty\,in}{K_I}$ is of 0.5% and for $\overset{\infty\,out}{K_I}$ it is unknown. In both cases, we show SIF results normalized by the reference solutions using the following formula

$$\bar{K} = \frac{K}{\overset{\infty}{K}}$$

where K is the stress intensity factor extracted from the hp-GFEM solution.

In the inner and outer crack examples, we apply strongly graded meshes along the crack front and uniform polynomial enrichment over the entire analysis domain. The resulting polynomial approximation order in both cases is $p = 3$. The same level of refinement is applied in both inner and outer crack examples. The ratios of element size to characteristic crack length, L_e/a and L_e/c, are around 0.053 and 0.014 for the inner and outer cracks respectively. This discretization is equivalent to the discretization applied on Mesh 3 of the example presented in Section 5.1. A Keast quadrature rule [12] with 45 points is used at each integration sub-element of the computational elements enriched with singular functions.

Figure 13(a) shows the computed stress intensity factor along the inner crack front. Table 4 lists the

22

absolute minimum, absolute maximum, average and standard deviation of the relative error along the crack front. The results show that enrichments computed with either crack front geometry approximation produce virtually identical solutions. They also show good agreement with the reference solution for semi-infinite domain. The average error for linear and quadratic crack front geometry approximations is around -0.22%. Moreover, the results show robustness of both crack front descriptions since the standard deviation of the error along the crack front is around 0.17%.

In Figure 13(b), we present the stress intensity factor for the simulation of a finite cylinder with outer crack. Table 4 lists the absolute minimum, absolute maximum, average and standard deviation of the relative error along the crack front. Again, the results for linear and quadratic crack front geometry approximations are almost identical and show good agreement with the reference solution for semi-infinite domain. Also, the results show that both approximations are very robust since the SIFs show small oscillations along the crack front. The average error along the crack front is, in this case, around 0.19% with standard deviation of 0.33%.

Table 4: Error analysis of SIF for inner and outer cracks in a finite cylinder.

Crack type	Crack front geom. Approximation	abs(min)	abs(max)	Error % average	std. deviation
Inner	Linear	0.009	0.605	-0.227	0.171
	Quadratic	0.002	0.632	-0.213	0.178
Outer	Linear	0.003	0.824	0.186	0.337
	Quadratic	0.005	0.845	0.188	0.329
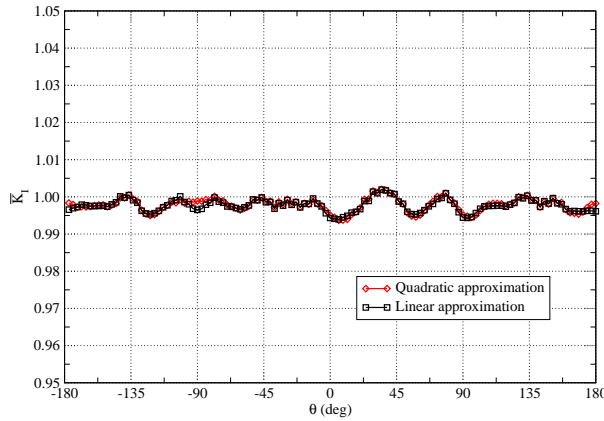
(a) Normalized SIF along crack front for a finite cylinder with inner crack
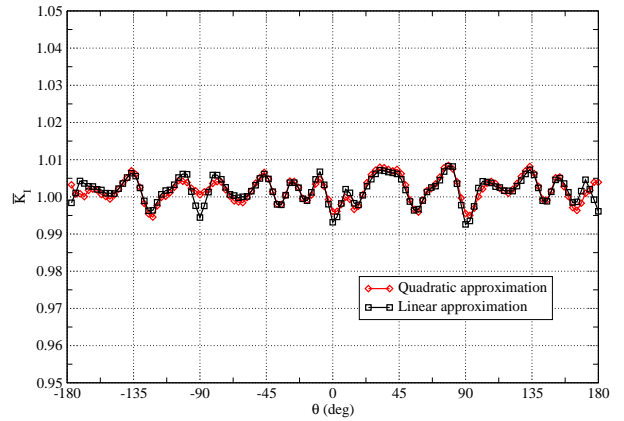
(b) Normalized SIF along crack front for a finite cylinder with outer crack

Figure 13: Normalized stress intensity factors (SIF) along the crack front for a finite cylinder with inner and outer cracks.

5.3 Inclined elliptical crack

The aim of this example is to verify the linear and quadratic crack front approximations in a problem with non-constant crack front curvature and mixed mode fracture behavior. The problem consists of an inclined elliptical crack of dimensions $a = 0.1$ and $b = 0.05$ embedded in a cube of edge size $2L$, as illustrated in

Figure14. In order to reduce the finite domain effect on the solution, we set $a/L = 10$. The material parameters used in this analysis are $E = 1.0 \times 10^3$ and $v = 0.30$. The slope of the crack with respect to the y-axis is $\gamma = \pi/4$. The domain is subjected to a uniform tensile traction $\sigma = 1$ in the y-axis. Figure 14 illustrates the model and the initial coarse mesh used in this example. In the discretization of the solution, we apply localized mesh refinement on GFEM elements that intersect the crack front and polynomial enrichment of order $p = 3$ over the entire domain. The range of the ratio of element size along the crack front, L_e, to characteristic crack length, a, is $0.018 \leq L_e/a \leq 0.041$. The crack surface is represented using a quasi uniform triangulation.

The stress intensity factors for modes I, II, and III of an inclined elliptical crack embedded in an infinite domain are used as reference. These SIFs are given by [38]

$$K_I^{\text{inf.}} = \frac{\sigma \sin^2 \gamma \sqrt{\pi b}}{E(k)} \left[\sin^2 \theta + \left(\frac{b}{a} \right)^2 \cos^2 \theta \right]^{\frac{1}{4}}$$

$$K_{II}^{\text{inf.}} = -\frac{\sigma \sin \gamma \cos \gamma \sqrt{\pi b} k^2}{\left[\sin^2 \theta + \left(\frac{b}{a} \right)^2 \cos^2 \theta \right]^{\frac{1}{4}}} \left[\frac{k'}{B} \cos \omega \cos \theta + \frac{1}{C} \sin \omega \sin \theta \right]$$

$$K_{III}^{\text{inf.}} = \frac{\sigma \sin \gamma \cos \gamma \sqrt{\pi b}(1-v) k^2}{\left[\sin^2 \theta + \left(\frac{b}{a} \right)^2 \cos^2 \theta \right]^{\frac{1}{4}}} \left[\frac{1}{B} \cos \omega \sin \theta - \frac{k'}{C} \sin \omega \cos \theta \right]$$

where B, C, $K(k)$ and $E(k)$ are defined as

$$B = (k^2 - v)E(k) + vk'^2 K(k), \quad C = (k^2 - vk'^2)E(k) - vk'^2 K(k),$$

$$K(k) = \int_0^{\frac{\pi}{2}} \frac{d\varphi}{\sqrt{1 - k^2 \sin^2 \varphi}}, \quad E(k) = \int_0^{\frac{\pi}{2}} \sqrt{1 - k^2 \sin^2 \varphi} d\varphi ,$$

and $k^2 = 1 - k'^2$, $k' = b/a$ and θ is a parametric angle representing a point A on the crack front (cf. Figure 14). For the example solved in this section, $\gamma = \pi/4$ and $\omega = \pi/2$.

Figure 15(a) and 15(b) illustrate the comparison of linear and quadratic crack front approximations with respect to the infinite domain solution, respectively. One can note that both approximations show good agreement with the infinite domain solution. Table 5 lists the normalized L^2-norm of the difference between the numerical solution and the reference solution (cf. Equation (20)). Like in the previous examples, we can observe that both approximations provide virtually the same results. The relative errors of the stress intensity factors along the crack front for linear and quadratic approximations show very small differences.

Table 5: Normalized L^2-norm of the error of the SIFs along the crack front for linear and quadratic approximations.

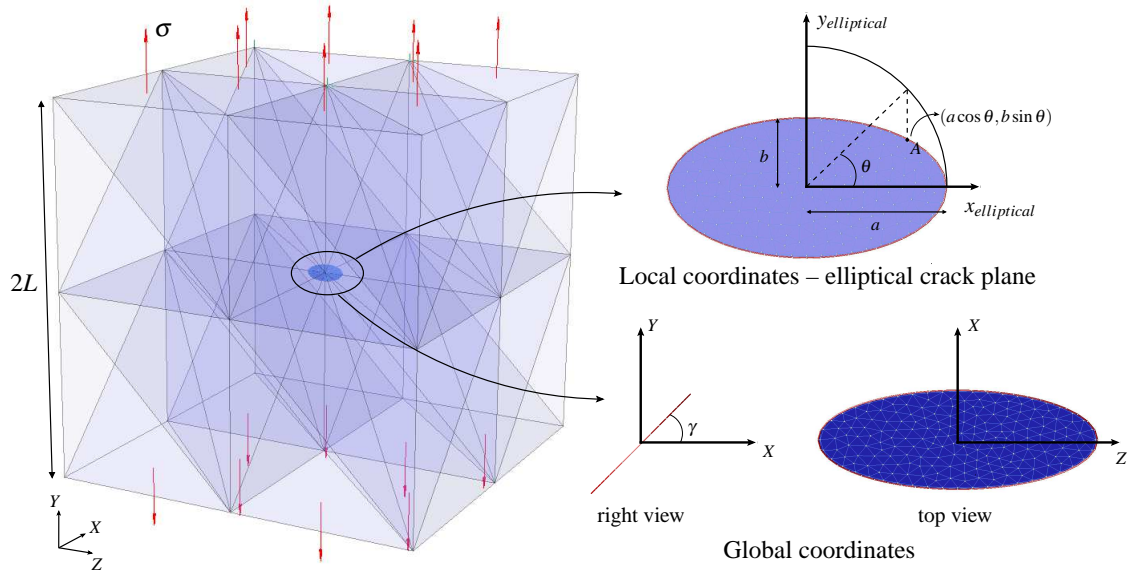| Crack front geom. approximation	$e^r(K_I)$	$e^r(K_{II})$	$e^r(K_{III})$
Linear	0.0234	0.00406	0.04133
Quadratic	0.0223	0.00486	0.04246

Figure 14: Cube subjected to top and bottom uniform tensile tractions and crack surface representation for inclined elliptical crack.

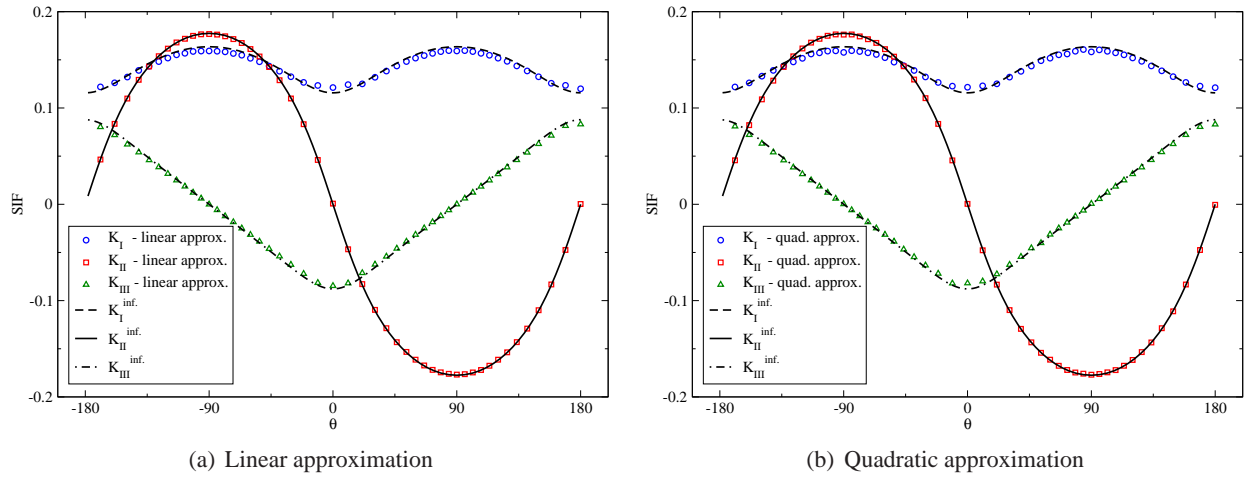(a) Linear approximation

(b) Quadratic approximation

Figure 15: Stress intensity factors for modes *I*, *II* and *III* using linear and quadratic crack front approximations.

6   Concluding remarks

Linear and quadratic approximations to represent curvilinear crack fronts are presented. These representations are geared towards the construction of enrichment functions for the generalized finite element. In both cases, special care is taken when setting the crack front coordinate system based on the geometric description of the crack front. The evaluation of crack front normals, tangents and conormals vectors using medial-quadric-based techniques ensures the robustness of the representation of the crack front geometry.

The results presented in Section 5 show that a coarse mesh with either linear or quadratic crack front geometry approximations leads to poor crack front description. As a result, the SIF solution along the crack front shows poor accuracy and very oscillatory behavior. However, by applying a suitable refinement level along the crack front the results show that both approaches lead to the same crack front representation in the limit case, i.e., when the crack front refinement is enough to capture the singular solution along the crack front.

The numerical experiments indicate that both crack front geometry approximations lead to very robust results in meshes typically used for this class of problem. The first approach uses Cartesian coordinate systems along the crack front and is straightforward to implement. The implementation of the second approach is more involved since it is based on curvilinear coordinate systems. Thus, *for the class of problems considered here*, the first approach is recommended.

The proposed approaches to build enrichment functions along curved crack fronts are not limited to the case of linear elastic fracture mechanics, the focus of this paper. Application of these approaches to the case of cohesive cracks, and other non-linear fracture mechanics problems is straightforward. The same procedure used to define the curvilinear coordinate system along the crack front can be used. The conclusions regarding which approach is better for other classes of problem may, of course, be different from the case considered here.

A Gradient of Enrichment Functions in Global Coordinates

This section presents the computation of the gradient of enrichment functions with respect to the global coordinates X_1, X_2, X_3. These quantities, in turn, are used in the computation of derivatives of GFEM shape functions defined in (1).

A.1 Case 1: Linear Approximation of Crack Front Geometry

In this section, we consider the case of the derivatives of the enrichment functions defined in Section 4.1.1.

Let $\bar{\boldsymbol{u}}(r,\theta)$ denote a displacement vector with components $(\bar{u}_1, \bar{u}_2, \bar{u}_3)$ where $\bar{u}_j$ equal to $\bar{L}_{\alpha 1}^{\xi_j}$ or $\bar{L}_{\alpha 2}^{\xi_j}$, for $j = 1,2,3$, and α arbitrary. Similarly, we define vectors $\hat{\boldsymbol{u}}(\xi_1, \xi_2, \xi_3)$ and $\boldsymbol{u}(X_1, X_2, X_3)$ using enrichment functions $\hat{L}_{\alpha i}^{\xi_j}(\xi_1, \xi_2, \xi_3)$ and $L_{\alpha i}^{X_j}, (X_1, X_2, X_3)$, $i = 1,2$, $j = 1,2,3$, respectively.

Let r_i, $i = 1,2,3$, denote cylindrical coordinates r, θ and ξ_3, respectively. The gradient of $\hat{\boldsymbol{u}}$ can be computed using the derivatives of the functions defined in (2) and is given by

$$\hat{\boldsymbol{u}}\overleftarrow{\nabla}_\xi = \frac{\partial \hat{u}_j}{\partial \xi_l}\hat{\boldsymbol{e}}_j \otimes \hat{\boldsymbol{e}}_l = \frac{\partial \bar{u}_j}{\partial r_m}\frac{\partial r_m}{\partial \xi_l}\hat{\boldsymbol{e}}_j \otimes \hat{\boldsymbol{e}}_l$$

where, from (6),

$$\frac{\partial r_m}{\partial \xi_l} = \left(\boldsymbol{J}_a^{-1}\right)_{ml}$$

The relation between the base vectors $\hat{\boldsymbol{e}}_m$, $m = 1,2,3$, of a Cartesian crack front coordinate system and the global based vectors $\boldsymbol{e}_i$, $i = 1,2,3$, is given by

$$\hat{\boldsymbol{e}}_m = \left(\boldsymbol{R}_b^{-1}\right)_{mi}\boldsymbol{e}_i$$

where $\boldsymbol{R}_b^{-1} = \boldsymbol{J}_b^{-1}$ (cf. Section 4.1.1).

Using the above, the gradient of $\boldsymbol{u}$ can be computed as follows

$$\begin{aligned}\hat{\boldsymbol{u}}\overleftarrow{\nabla}_\xi &= \frac{\partial \hat{u}_m}{\partial \xi_n}\hat{\boldsymbol{e}}_m \otimes \hat{\boldsymbol{e}}_n = \frac{\partial \hat{u}_m}{\partial \xi_n}\left(\boldsymbol{R}_b^{-1}\right)_{mi}\boldsymbol{e}_i \otimes \left(\boldsymbol{R}_b^{-1}\right)_{nj}\boldsymbol{e}_j \\ &= \left(\boldsymbol{R}_b^{-1}\right)_{mi}\frac{\partial \hat{u}_m}{\partial \xi_n}\left(\boldsymbol{R}_b^{-1}\right)_{nj}\boldsymbol{e}_i \otimes \boldsymbol{e}_j = \frac{\partial u_i}{\partial X_j}\boldsymbol{e}_i \otimes \boldsymbol{e}_j = \boldsymbol{u}\overleftarrow{\nabla}_X\end{aligned}$$

Thus, the derivatives of the enrichment functions with respect to global coordinates can be computed using

$$\frac{\partial u_i}{\partial X_j} = \left(\boldsymbol{R}_b^{-1}\right)_{mi}\frac{\partial \hat{u}_m}{\partial \xi_n}\left(\boldsymbol{R}_b^{-1}\right)_{nj}$$

In matrix form, we have

$$\left[\boldsymbol{u}\overleftarrow{\nabla}_X\right] = \boldsymbol{R}_b\left[\hat{\boldsymbol{u}}\overleftarrow{\nabla}_\xi\right]\boldsymbol{R}_b^T.$$

A.2 Case 2: Quadratic Approximation of Crack Front Geometry

The case of enrichment functions defined using a quadratic approximation of the crack front geometry follows the same steps as in the section above. However, in this case, the coordinate system is curvilinear. The computation of the gradient of the displacement vector with respect to curvilinear coordinates must also

consider the derivatives of the crack front base vectors and scale factors. This is presented below in Sections A.2.1 and A.2.2, respectively.

A.2.1 Derivatives of crack front base vectors

In general, the base vectors of a curvilinear system vary in length and orientation from point to point in space. In an orthonormal system the length of the vectors is always unit, but their orientations may change. Therefore, a curvilinear orthonormal base system can be regarded as a triad that rigidly rotates from point to pont in the curvilinear space.

The derivatives of a curvilinear orthonormal basis can be written as follows [15]

$$\frac{\partial \hat{\boldsymbol{e}}_j}{\partial \xi_i} = \left[\frac{\delta_{ik}}{\hat{h}_j} \frac{\partial \hat{h}_i}{\partial \xi_j} - \frac{\delta_{ij}}{\hat{h}_k} \frac{\partial \hat{h}_j}{\partial \xi_k} \right] \hat{\boldsymbol{e}}_k \tag{21}$$

All sections $\xi_3 = C$, where C is a constant, of the 12-node hexahedron element used in the definition of curvilinear coordinate systems (cf. Section 4.2.1) have the following properties

- They are squared, i.e., there is no distortion on the $\xi_1 \, \xi_2$ plane;

- all section have the same dimensions;

- they are planar, i.e. there is no warping on the $\xi_1 \, \xi_2$ plane.

Based on these assumptions, the base vectors $\hat{\boldsymbol{e}}_j$, $j = 1, 2, 3$, are dependent on ξ_3 only and all scaling factors are constant, except $\hat{h}_3$.

Depending on the nodal coordinates of the element, however, sections $\xi_3 = C$ may be non-orthogonal to the coordinate line ξ_3. This happens if the element has a large curvature in the ξ_3 direction. The procedure presented in Section 4.2.1, however, keeps this distortion to a minimum. Furthermore, even when the element is distorted, this is much less pronounced near the centroid of the element. The enriched cloud (ω_α) is located, by construction, almost at the center of the hexahedron. Therefore, it is reasonable to assume that the base vectors $\hat{\boldsymbol{e}}_j$, $j = 1, 2, 3$, form an orthonormal basis over the enriched cloud (ω_α).

Based on the above, the derivatives of the base vectors $\hat{\boldsymbol{e}}_j$, $j = 1, 2, 3$, reduce to

$$\frac{\partial \hat{\boldsymbol{e}}_1}{\partial \xi_3} = \frac{1}{\hat{h}_1} \frac{\partial \hat{h}_3}{\partial \xi_1} \hat{\boldsymbol{e}}_3 \tag{22}$$

$$\frac{\partial \hat{\boldsymbol{e}}_2}{\partial \xi_3} = \frac{1}{\hat{h}_2} \frac{\partial \hat{h}_3}{\partial \xi_2} \hat{\boldsymbol{e}}_3 \tag{23}$$

$$\frac{\partial \hat{\boldsymbol{e}}_3}{\partial \xi_3} = -\frac{1}{\hat{h}_1} \frac{\partial \hat{h}_3}{\partial \xi_1} \hat{\boldsymbol{e}}_1 - \frac{1}{\hat{h}_2} \frac{\partial \hat{h}_3}{\partial \xi_2} \hat{\boldsymbol{e}}_2 \tag{24}$$

and all other components are zero.

A.2.2 Derivatives of the scale factors

The derivatives the scale factors defined in (13) can be written as follows.

$$\frac{\partial \hat{h}_j}{\partial \xi_i} = \frac{1}{\hat{h}_j} \frac{\partial \hat{\boldsymbol{g}}_j}{\partial \xi_i} \cdot \hat{\boldsymbol{g}}_j = \frac{1}{\hat{h}_j} \frac{\partial^2 X_k}{\partial \xi_i \partial \xi_j} \frac{\partial X_k}{\partial \xi_j} \tag{25}$$

with no summation on j.

Based on the discussion in the previous section, only the following terms are non-zero

$$\frac{\partial \hat{h}_3}{\partial \xi_1} = \frac{1}{\hat{h}_3} \frac{\partial^2 X_k}{\partial \xi_1 \partial \xi_3} \frac{\partial X_k}{\partial \xi_3} \tag{26}$$

$$\frac{\partial \hat{h}_3}{\partial \xi_2} = \frac{1}{\hat{h}_3} \frac{\partial^2 X_k}{\partial \xi_2 \partial \xi_3} \frac{\partial X_k}{\partial \xi_3}. \tag{27}$$

A.2.3 Gradient of the displacement field

Let $\hat{\boldsymbol{u}}$ be a displacement vector with components given by enrichment functions $\hat{L}_{\alpha n}^{\xi_i}(\xi_1, \xi_2, \xi_3)$, $n = 1$ or $n = 2$ and $i = 1, 2, 3$, as in Section A.1. The gradient of $\hat{\boldsymbol{u}}$ with respect to curvilinear coordinates ξ_1, ξ_2, ξ_3 can be computed using [30]

$$
\begin{aligned}
\hat{\boldsymbol{u}} \overleftarrow{\nabla}_\xi &= \hat{u}_j \hat{\boldsymbol{e}}_j \otimes \frac{\overleftarrow{\partial}}{\partial \xi_i} \hat{\boldsymbol{e}}_i \frac{1}{\hat{h}_i} = (\hat{u}_1 \hat{\boldsymbol{e}}_1 + \hat{u}_2 \hat{\boldsymbol{e}}_2 + \hat{u}_3 \hat{\boldsymbol{e}}_3) \otimes \left(\frac{\overleftarrow{\partial}}{\partial \xi_1} \hat{\boldsymbol{e}}_1 \frac{1}{\hat{h}_1} + \frac{\overleftarrow{\partial}}{\partial \xi_2} \hat{\boldsymbol{e}}_2 \frac{1}{\hat{h}_2} + \frac{\overleftarrow{\partial}}{\partial \xi_3} \hat{\boldsymbol{e}}_3 \frac{1}{\hat{h}_3} \right) \\
&= \frac{1}{\hat{h}_i} \frac{\partial \hat{u}_j}{\partial \xi_i} \hat{\boldsymbol{e}}_j \otimes \hat{\boldsymbol{e}}_i + \frac{\hat{u}_j}{\hat{h}_i} \frac{\partial \hat{\boldsymbol{e}}_j}{\partial \xi_i} \otimes \hat{\boldsymbol{e}}_i
\end{aligned}
\tag{28}
$$

In indicial notation, we have

$$\left(\hat{\boldsymbol{u}} \overleftarrow{\nabla}_\xi \right)_{ki} = \frac{1}{\hat{h}_i} \left(\frac{\partial \hat{u}_k}{\partial \xi_i} + \frac{\hat{u}_j}{\hat{h}_j} \frac{\partial \hat{h}_i}{\partial \xi_j} \delta_{ik} - \frac{\hat{u}_i}{\hat{h}_k} \frac{\partial \hat{h}_i}{\partial \xi_k} \right)$$

Using $\dfrac{\partial \hat{u}_k}{\partial \xi_i} = \dfrac{\partial \bar{u}_k}{\partial r_l} \dfrac{\partial r_l}{\partial \xi_i}$, where $\dfrac{\partial r_l}{\partial \xi_i} = \left(\boldsymbol{J}_2^{-1} \right)_{li}$, we have

$$\left(\hat{\boldsymbol{u}} \overleftarrow{\nabla}_\xi \right)_{ki} = \frac{1}{\hat{h}_i} \left(\underbrace{\frac{\partial \bar{u}_k}{\partial r_l} \frac{\partial r_l}{\partial \xi_i}}_{\text{derivatives of displacements}} + \underbrace{\frac{\hat{u}_j}{\hat{h}_j} \frac{\partial \hat{h}_i}{\partial \xi_j} \delta_{ik} - \frac{\hat{u}_i}{\hat{h}_k} \frac{\partial \hat{h}_i}{\partial \xi_k}}_{\text{derivatives of vectors}} \right) \tag{29}$$

where $\bar{u}_k, k = 1, 2, 3$, are the components of vector $\bar{\boldsymbol{u}}$ defined in Section A.1. The indices of the scale factors do not take part in the summation convention.

Using the results from Sections A.2.1 and A.2.2, we can write the components of the gradient of the displacement vector $\hat{\boldsymbol{u}}$ in matrix form

$$
\left[\hat{\boldsymbol{u}} \overleftarrow{\nabla}_\xi \right] =
\begin{bmatrix}
\dfrac{1}{\hat{h}_1} \dfrac{\partial \hat{u}_1}{\partial \xi_1} & \dfrac{1}{\hat{h}_2} \dfrac{\partial \hat{u}_1}{\partial \xi_2} & \dfrac{1}{\hat{h}_3} \dfrac{\partial \hat{u}_1}{\partial \xi_3} \\[2mm]
\dfrac{1}{\hat{h}_1} \dfrac{\partial \hat{u}_2}{\partial \xi_1} & \dfrac{1}{\hat{h}_2} \dfrac{\partial \hat{u}_2}{\partial \xi_2} & \dfrac{1}{\hat{h}_3} \dfrac{\partial \hat{u}_2}{\partial \xi_3} \\[2mm]
\dfrac{1}{\hat{h}_1} \dfrac{\partial \hat{u}_3}{\partial \xi_1} & \dfrac{1}{\hat{h}_2} \dfrac{\partial \hat{u}_3}{\partial \xi_2} & \dfrac{1}{\hat{h}_3} \dfrac{\partial \hat{u}_3}{\partial \xi_3}
\end{bmatrix}
+
\begin{bmatrix}
0 & 0 & -\dfrac{\hat{u}_3}{\hat{h}_3} \dfrac{1}{\hat{h}_1} \dfrac{\partial \hat{h}_3}{\partial \xi_1} \\[2mm]
0 & 0 & -\dfrac{\hat{u}_3}{\hat{h}_3} \dfrac{1}{\hat{h}_2} \dfrac{\partial \hat{h}_3}{\partial \xi_2} \\[2mm]
0 & 0 & \dfrac{\hat{u}_1}{\hat{h}_1} \dfrac{1}{\hat{h}_3} \dfrac{\partial \hat{h}_3}{\partial \xi_1} + \dfrac{\hat{u}_2}{\hat{h}_2} \dfrac{1}{\hat{h}_3} \dfrac{\partial \hat{h}_3}{\partial \xi_2}
\end{bmatrix}
\tag{30}
$$

We can now compute the gradient of the enrichment functions with respect to global coordinates using the same steps as in Section A.1.

The relation between the base vectors $\hat{\boldsymbol{e}}_m$, $m = 1, 2, 3$, of a curvilinear crack front coordinate system and

the global based vectors $\mathbf{e}_i$, $i = 1, 2, 3$ is given by

$$\hat{\mathbf{e}}_m = \left(\mathbf{R}_1^{-1} \right)_{mi} \mathbf{e}_i$$

where $\mathbf{R}_1^{-1}$ is a rotation matrix with rows given by the base vectors $\hat{\mathbf{e}}_i$, $i = 1, 2, 3$, defined in Section 4.2.2, i.e.,

$$\left(\mathbf{R}_1^{-1} \right)_{ij} = \frac{1}{\hat{h}_i} \frac{\partial X_j}{\partial \xi_i}$$

This transformation tensor is dependent on ξ_3, the position along the crack front. Again, no summation is implied over the indice i of the scale factors.

Using the above

$$\left(\mathbf{u} \overleftarrow{\nabla}_X \right)_{ij} = \left(\mathbf{R}_1^{-1} \right)_{mi} \left(\hat{\mathbf{u}} \overleftarrow{\nabla}_\xi \right)_{mn} \left(\mathbf{R}_1^{-1} \right)_{nj}$$

where $\left(\hat{\mathbf{u}} \overleftarrow{\nabla}_\xi \right)_{mn}$ are the components of the gradient of the displacement vector $\hat{\mathbf{u}}$ in the curvilinear system as defined in (29) and $\left(\mathbf{u} \overleftarrow{\nabla}_X \right)_{ij}$ are the gradient components in global coordinates.

In matrix form, we have

$$\left[\mathbf{u} \overleftarrow{\nabla}_X \right] = \mathbf{R}_1 \left[\hat{\mathbf{u}} \overleftarrow{\nabla}_\xi \right] \mathbf{R}_1^T.$$

References

[1] I. Babuška and J.M. Melenk. The partition of unity finite element method. *International Journal for Numerical Methods in Engineering*, 40:727–758, 1997. 1, 3

[2] T. Belytschko and T. Black. Elastic crack growth in finite elements with minimal remeshing. *International Journal for Numerical Methods in Engineering*, 45:601–620, 1999. 2

[3] D.L. Chopp and N. Sukumar. Fatigue crack propagation of multiple coplanar cracks with the coupled extended finite element/fast marching method. *International Journal of Engineering Science*, 41:845–869, 2003. 4

[4] C.A. Duarte, I. Babuška, and J.T. Oden. Generalized finite element methods for three dimensional structural mechanics problems. *Computers and Structures*, 77:215–232, 2000. 1, 2, 3, 4, 10

[5] C.A. Duarte, O.N. Hamzeh, T.J. Liszka, and W.W. Tworzydlo. A generalized finite element method for the simulation of three-dimensional dynamic crack propagation. *Computer Methods in Applied Mechanics and Engineering*, 190(15-17):2227–2262, 2001. http://dx.doi.org/10.1016/S0045-7825(00)00233-4. 2, 3, 4

[6] C.A. Duarte, L.G. Reno, and A. Simone. A high-order generalized FEM for through-the-thickness branched cracks. *International Journal for Numerical Methods in Engineering*, 72(3):325–351, 2007. http://dx.doi.org/10.1002/nme.2012. 2

[7] C.A.M. Duarte and J.T. Oden. An *hp* adaptive method using clouds. *Computer Methods in Applied Mechanics and Engineering*, 139:237–262, 1996. 2

[8] M. Duflot. A study of the representation of cracks with level sets. *International Journal for Numerical Methods in Engineering*, 70:1261–1302, 2007. 5

[9] M. Fleming, Y. A. Chu, B. Moran, and T. Belytschko. Enriched element-free Galerkin methods for crack tip fields. *International Journal for Numerical Methods in Engineering*, 40:1483–1504, 1997. 2

[10] X. Jiao. Face offsetting: A unified framework for explicit moving interfaces. *Journal of Computational Physics*, 220(2):612–625, 2007. 6

[11] X. Jiao, N. R. Bayyana, and H. Zha. Optimizing surface triangulation via near isometry with reference meshes. In Y. S. Geert, D. van Albada, J. Dongarra, and P. M. A. Sloot, editors, *Computational Science – ICCS 2007*, pages 334–341, Beijing, China, May 2007. Springer. Proceedings, Part I. 6

[12] P. Keast. Moderate-degree tetrahedral quadrature formulas. *Computer Methods in Applied Mechanics and Engineering*, 55:339–348, 1986. 17, 22

[13] P. Lancaster and K. Salkauskas. Surfaces generated by moving least squares methods. *Mathematics of Computation*, 37(155):141–158, 1981. 2

[14] P. Lancaster and K. Salkauskas. *Curve and Surface Fitting, an Introduction*. Academic Press, San Diego, 1986. 2

[15] L.P. Lebedev and M.J. Cloud. *Tensor Analysis*. World Scientific, New Jersey, 2003. 28

[16] J.M. Melenk and I. Babuška. The partition of unity finite element method: Basic theory and applications. *Computer Methods in Applied Mechanics and Engineering*, 139:289–314, 1996. 1, 3

[17] J. Mergheim, E. Kuhl, and P. Steinmann. A finite element method for the computational modeling of cohesive cracks. *International Journal for Numerical Methods in Engineering*, 63:276–289, 2005. 2

[18] N. Moës and T. Belytschko. Extended finite element method for cohesive crack growth. *Engineering Fracture Mechanics*, 69:813–833, 2002. 2

[19] N. Moës, J. Dolbow, and T. Belytschko. A finite element method for crack growth without remeshing. *International Journal for Numerical Methods in Engineering*, 46:131–150, 1999. 2

[20] N. Moës, A. Gravouil, and T. Belytschko. Non-planar 3D crack growth by the extended finite element and level sets – Part I: Mechanical model. *International Journal for Numerical Methods in Engineering*, 53(11):2549–2568, 2002. 2, 4, 5

[21] Y. Murakami. *Stress intensity factors handbook*, volume 3. Pergamon, Oxford, New York, 1st edition, 1992. 22

[22] J.T. Oden and C.A. Duarte. Chapter: Clouds, Cracks and FEM's. In B.D. Reddy, editor, *Recent Developments in Computational and Applied Mechanics*, pages 302–321, Barcelona, Spain, 1997. International Center for Numerical Methods in Engineering, CIMNE. 2, 3, 4

[23] J.T. Oden, C.A. Duarte, and O.C. Zienkiewicz. A new cloud-based *hp* finite element method. *Computer Methods in Applied Mechanics and Engineering*, 153:117–126, 1998. 1, 3

[24] J.T. Oden and C.A.M. Duarte. Chapter: Solution of singular problems using *hp* clouds. In J.R. Whiteman, editor, *The Mathematics of Finite Elements and Applications– Highlights 1996*, pages 35–54, New York, NY, 1997. John Wiley & Sons. 2, 3, 4

[25] K. Park, J.P. Pereira, C.A. Duarte, and G.H. Paulino. Integration of singular enrichment functions in the generalized/extended finite element method for three-dimensional problems. *International Journal for Numerical Methods in Engineering*, 2008. Accepted for publication. 4, 17

[26] J.P. Pereira and C.A. Duarte. Computation of stress intensity factors for pressurized cracks using the generalized finite element method and superconvergent extraction techniques. In P.R.M. Lyra, S.M.B.A. da Silva, F.S. Magnani, L.J. do N. Guimaraes, L.M. da Costa, and E. Parente Junior, editors, *XXV Iberian Latin-American Congress on Computational Methods in Engineering*, Recife, PE, Brazil, November 2004. 15 pages. ISBN Proceedings CD: 857 409 869-8. 16

[27] J.P. Pereira and C.A. Duarte. Extraction of stress intensity factors from generalized finite element solutions. *Engineering Analysis with Boundary Elements*, 29:397–413, 2005. 16

[28] J.P. Pereira, C.A. Duarte, D. Guoy, and X. Jiao. *Hp*-Generalized FEM and crack surface representation for non-planar 3-D cracks. *International Journal for Numerical Methods in Engineering*, 2008. http://dx.doi.org/10.1002/nme.2419. 2, 3, 4, 5, 10, 16, 17, 18

[29] J.C. Raju, I.S. Newman Jr. Stress-intensity factors for a wide range of semi-elliptical surface cracks in finite-thickness plates. *Engineering Fracture Mechanics*, 11:817–829, 1979. 17

[30] J.N. Reddy and M.L. Rasmussen. *Advanced Engineering Analysis*. John Wiley and Sons, New York, 1982. 29

[31] A. Simone. Partition of unity-based discontinuous elements for interface phenomena: Computational issues. *Communications in Numerical Methods in Engineering*, 20:465–478, 2004. 2

[32] A. Simone, G.N. Wells, and L.J. Sluys. From continuous to discontinuous failure in a gradient-enhanced continuum damage model. *Computer Methods in Applied Mechanics and Engineering*, 192(41-42):4581–4607, 2003. 2

[33] T. Strouboulis, K. Copps, and I. Babuška. The generalized finite element method. *Computer Methods in Applied Mechanics and Engineering*, 190:4081–4193, 2001. 1, 3

[34] N. Sukumar, D.L. Chopp, and B. Moran. Extended finite element method and fast marching method for three-dimensional fatigue crack propagation. *Engineering Fracture Mechanics*, 70:29–48, 2003. 4, 5

[35] N. Sukumar, N. Moës, B. Moran, and T. Belytschko. Extended finite element method for three-dimensional crack modelling. *International Journal for Numerical Methods in Engineering*, 48(11):1549–1570, 2000. 2, 4, 5

[36] B. Szabo and I. Babuška. *Finite Element Analysis*. John Wiley and Sons, New York, 1991. 4, 16, 20

[37] B. A. Szabo and I. Babuška. Computation of the amplitude of stress singular terms for cracks and reentrant corners. In T.A. Cruse, editor, *Fracture Mechanics: Nineteenth Symposium, ASTM STP 969*, pages 101–124, Southwest Research Institute, San Antonio, TX, 1988. 16

[38] H. Tada, P. Paris, and G. Irwin. *The Stress Analysis of Cracks Handbook*. ASME Press, New York, 3rd edition, 2000. 22, 24

[39] M. C. Walters, G. H. Paulino, and R. H. Dodds Jr. Stress-intensity factors for surface cracks in functionally graded materials under mode-I thermomechanical loading. *International Journal of Solids and Structures*, 41:1081–1118, 2004. 17, 20

[40] G.N. Wells, R. de Borst, and L.J. Sluys. A consistent geometrically non-linear approach for delamination. *International Journal for Numerical Methods in Engineering*, 54:1333–1355, 2002. 2

[41] G.N. Wells and L.J. Sluys. A new method for modeling cohesive cracks using finite elements. *International Journal for Numerical Methods in Engineering*, 50:2667–2682, 2001. 2

[42] G. Zi and T. Belytschko. New crack-tip elements for XFEM and applications to cohesive cracks. *International Journal for Numerical Methods in Engineering*, 57:2221–2240, 2003. 2